

Influences of Cost Reduction Measures on the Beam Quality of a Large-Area Heliostat



Diploma Thesis

Steffen Ulmer
Matrikel-Nr. 1648377

Tutors: Gerhard Weinrebe (IER)
and Peter Heller (PSA)

1.2.98 – 20.12.98
Plataforma Solar de Almería, Spain

Abstract

The specific costs of heliostats and with them the levelized electricity costs (LEC) of solar power tower plants can be reduced significantly by increasing the size of the reflective area per heliostat from the usual 40 – 60 m² to more than 100 m² (so-called large-area heliostats). However, there can occur structural problems that decrease the optical performance through a day. The present study examines and analyses the beam quality of the GM-100, a large-area heliostat designed by the Spanish Center of Energy and Environmental Technologies (CIEMAT) and erected on the Plataforma Solar de Almería (PSA). To inquire the daily focus development on a target and the deformations of the mirror plane, various measurements with a digital camera, a laser beam and a temperature probe were taken. With a simplified mathematical model of the support structure with acting loads and temperature gradients, the deformations and the resulting focus development were also inquired theoretically. The calculated results were well consistent with the measured results and showed that the main reason for the unsatisfactory beam quality was the high deformation of the torque, as well due to the gravitational loads as to the temperature gradients. With this know-how, several well-aimed improvements were suggested. The idea of a stay pole construction was then specified, planned and constructed. The expected reduction of the deformations by about 60 % was even topped by the measurements. In addition, the developed construction gave the possibility to save about 1400 kg of steel.

Kurzfassung

Die Vergrößerung der Spiegelfläche von Heliostaten von bisher 40 bis maximal 60 m² auf über 100 m² (sogenannte Large-Area Heliostats) birgt ein großes Senkungspotential der spezifischen Heliostat-Kosten und damit der Stromerzeugungskosten solarer Turmkraftwerke. Dabei können allerdings strukturelle Probleme auftreten, die die optische Qualität im Tagesverlauf beeinträchtigen. Die vorliegende Arbeit untersucht und analysiert die Beamquality des vom spanischen Zentrum für Energie und Umwelttechnologien (CIEMAT) entwickelten und auf der Plataforma Solar de Almería (PSA) errichteten Large-Area Heliostaten GM-100. Um den Focus-Tagesverlauf auf einem Target und die Verformungen der Spiegelfläche zu ermitteln, wurden verschiedene Messungen mit Digitalkamera, Laserstab und Temperaturfühler durchgeführt. Ein vereinfachtes mathematisches Modell der Tragestruktur und der herrschenden Kräfte und Temperaturverteilungen wurde erstellt und damit die Verformungen und der resultierende Focusverlauf theoretisch ermittelt. Die errechneten und gemessenen Ergebnisse wiesen eine gute Übereinstimmung auf und zeigten, daß die Hauptursache der unbefriedigenden Focusqualität in der starken Durchbiegung des Querrohres sowohl aufgrund des Gewichtes als auch der Temperaturverteilung lag. Mit diesem Wissen konnten gezielte Verbesserungsvorschläge gemacht werden. Die Idee einer Drahtseilabspannung wurde weiterverfolgt, ausgearbeitet und praktisch umgesetzt. Die erwartete Verringerung der Verbiegungen um 60 % wurde durch dieselben Messungen sogar noch übertroffen. Weiterhin ergab sich durch die Konstruktion noch eine mögliche Einsparung von circa 1400 kg Stahl.

1 Introduction	9
2 State of the Art in Thermal Solar Power Plant Technology	11
2.1 Overview.....	11
2.2 Solar Tower Power Plants (Central Receiver Systems).....	12
2.2.1 Heliostat Field.....	13
2.2.2 Receivers.....	14
2.2.3 The PHOEBUS Concept.....	15
3 Costs and Potential of Cost Reduction	17
3.1 Solar Tower Power Plants.....	17
3.2 Heliostats.....	19
3.2.1 Development and Potential of Cost Reduction.....	20
3.2.2 Consequences of Cost Reduction Measures on Beam Quality.....	22
4 The GM-100 Glass-Mirror Heliostat	25
4.1 General Description.....	25
4.2 Performance and Beam Quality.....	26
4.3 Reasons for and Influences on Observed Performance.....	28
4.3.1 Exterior Influences.....	28
4.3.2 Effects on Structural Parts.....	29
4.4 Mathematical Models for GM-100 Behaviour.....	29
4.4.1 Gravity Loads of the Pedestal.....	30
4.4.2 Gravity Loads of the Torque Tube.....	31
4.4.3 Gravity Loads of the Trusses.....	34
4.4.4 Temperature Influence.....	36
4.4.5 Wind Loads.....	37
4.4.6 Superimposed Deformations.....	37
5 Measurement Set-Up	38
5.1 Set-Up of the Laser Measurements.....	38
5.2 Temperature Measurements.....	39
5.3 Flux Measurement.....	40
6 Results	42
6.1 Measurements Results and Assessment.....	42
6.1.1 Deformation of the Torque Tube.....	42
1.1.2 Measured Surface Temperature Development.....	43
1.1.3 Deformation due to Spatial Temperature Gradient.....	44
1.1.4 Daily Focus Development.....	45
1.1.5 Pictures of Reflected Rays.....	47
1.2 Results of Calculations.....	47
1.2.1 Deformation of Support Structure.....	47
1.2.2 Daily Focus Development.....	52

1.3	Influences of Cost Reduction Measures on Beam Quality	55
1.4	Improvements of Construction	56
1.4.1	Protection from direct Insolation	56
1.4.2	Modification of the Torque Tube.....	56
1.4.3	Stay Pole.....	56
1.4.4	Composite Materials	57
1.4.5	Estimated Effects	57
7	Realization of Constructive Improvements.....	60
7.1	Planning of the Construction	60
7.2	Building of the Construction.....	62
7.3	The Testing of the Improved Construction	65
8	Summary and Outlook	71
9	References.....	73
Appendix	75

Table of Figures

Fig. 2-1:	The three concepts of concentrating solar thermal electricity generation	11
Fig. 2-1:	The two large area heliostats tested at the PSA: GM-100 (left), ASM-150 (right).....	14
Fig. 2-1:	Principle of the PHOEBUS solar power plant.....	16
Fig. 3-1:	Estimated Future Investment Cost Structure of a 100 MW Tower SPP with 7h Storage /WINTER 1991/	18
Fig. 3-2:	Sensitivity Analysis of the LEC on various Parameters	19
Fig. 3-1:	Status and Trends in Heliostat Development: Technology, Configuration, Specific Weight and Specific Costs.....	21
Fig. 4-1:	Front and lateral views of GM-100 heliostat.	25
Fig. 4-1a and b:	GM-100 split focus at noon, 4 months later from canting point.....	27
Fig. 4-2a and b:	GM-100 split focus early in the morning.....	27
Fig. 4-1:	Definitions of the used Coordinate System.....	30
Fig. 4-1:	Simplified Model of the Pedestal.....	31
Fig. 4-1:	Simplified Model of one Side of the Torque Tube	32
Fig. 4-2:	Bending Line of Torque Tube due to Gravity.....	34
Fig. 4-1:	Simplified Model of the Truss	35
Fig. 4-2:	Bending line of truss	35
Fig. 4-1:	Bending of a Tube due to a Temperature Gradient over the cross-section of the tube.....	36
Fig. 5-1:	Set-up of the new Laser Canting Methodology	38
Fig. 5-2:	Laser Measurement Points	39
Fig. 5-1:	Set-up of Temperature Measurements	40
Fig. 5-1:	PROHERMES Flux Measurement Set-up	41
Fig. 6-1:	Development of Surface Temperatures on June 9 th 1998	44
Fig. 6-1:	GM-100 Daily Focus Development (time in brackets relative to solar noon).....	46
Fig. 6-1:	Reflected rays of the GM-100 early in the morning	47
Fig. 6-1:	GM-100 deformation at 40° elevation, 3 K temperature difference in torque tube and in pedestal	48
Fig. 6-2:	GM-100 deformation at 0° elevation, 0 K temperature difference	49
Fig. 6-3:	GM-100 deformation at 90° elevation, 0 K temperature difference	50
Fig. 6-4:	GM-100 deformation with 5.3 K temperature difference in the torque tube and 3.3 K in the pedestal without gravitational influences.....	51
Fig. 6-1:	Calculated Daily Focus Development of the GM-100 (time in brackets relative to solar noon)	54
Fig. 6-1:	Beam Quality due to Structural Deformations versus Heliostat Size	55
Fig. 6-1:	Effects of Design Improvements.....	58
Fig. 7-1:	Overview of the Stay Pole Construction	60
Fig. 7-1:	The completely assembled Stay Pole Construction	64
Fig. 7-1:	Calculated Focus Development for modified GM-100 on December 10 th 1998.....	67
Fig. 7-2:	Calculated Focus Development of the Modified GM-100 on June, 9 th and July, 7 th resp.....	68
Fig. 7-3:	Comparison of Calculated Focus Shapes close to Sunset (6.7.1998, 19:44h, DNI = 1.0 kW/m ²)	70

Table of Tables

Table 2-1:	Test Facilities and Pilot plants 1997	12
Table 3-1:	Cost Estimates for Second Generation Towers	17
Table 4-1:	Characteristics of the GM-100.....	26
Table 6-1:	Results of the Deformation Measurements on April, 21 st , 1998.....	43
Table 6-1:	Results of the Temperature Measurements on June, 9 th , 1998	43
Table 6-1:	Results of the Temperature and Deformation Measurements on June, 2 nd , 1998.....	45
Table 6-1:	Selected Results of Deformation Calculations and Measurements	52
Table 6-1:	Input Data for Calculation of Focus Development (Estimated ΔT at canting time: 3.0 K)	53
Table 6-1:	Comparison of the Material Requirements of Large-Area Heliostats	59
Table 7-1:	Calculated Forces acting in the Staypole Construction	61
Table 7-2:	Written Order for Construction Parts.....	62
Table 7-1:	Measured and Calculated Deformations of Improved GM-100	65
Table 7-2:	Results of the Temperature Measurements on November, 26 th , 1998.....	65
Table 7-3:	Sun Positions on December 10 th 1998	66

Symbols

a	distance from the center of gravity of a truss to the torque tube center
$A_{concentrator}$	concentrator area
A_{tube}	cross sectional area of torque tube
D_{ped}	diameter of pedestal
D_{tube}	diameter of torque tube
e	length of lever of elevation drive
E	Young's modulus
$elev$	heliostat elevation angle
F_{bar}	acting force in bar
$F_{bearing}$	reaction force in the torque tube bearing
F_{cable}	acting force in cable
F_{conc}	gravity force of the concentrator
F_{max}	maximum load
F_{pole}	force acting in stay pole
F_{truss}	gravity force of one truss with facets
$F_{w,frontal}$	wind force acting on heliostat
g	gravitational constant
G	shear modulus
I	moment of inertia
$I(x,y)$	irradiance distribution
I_p	axial moment of inertia
l_{1-4}	distances of the trusses to the center
$l_{bearing}$	distance of torque tube bearings to the center
l_k	effective column length
L_{ped}	length of pedestal
L_{tube}	length of torque tube
$M(x)$	inner moment
$M_{b,ped}$	bending moment acting on pedestal
$M_{b,tube}$	inner moment of the torque tube
M_{truss}	torque from one truss acting on the torque tube
m_{tube}	mass of the torque tube
$m_{xfacets}$	mass of the x facets
$m_{xtrusses}$	mass of the x trusses
p	exponent used in definition
$q(x)$	specific length load
$Q(x)$	transverse force
q_{truss}	area load of the facets acting on the truss
q_{tube}	area load due to the torque tube's deadweight
R	radius of the arc of the bent tube
S_{bar}	safety factor in bar
S_{cable}	safety factor in cable
S_{pole}	safety factor of pole
t_{ped}	wall thickness of pedestal

t_{tube}	wall thickness of torque tube
v_{wind}	wind velocity
$w(x)$	bending line
$w'(x)$	gradient of the bending line
x, y, z	coordinates
x_g, y_g	coordinates of the beam centroid
$\Delta z_{ped,g}$	z-displacement due to the bending of the pedestal caused by gravity loads
$\Delta z_{ped,t}$	z-displacement due to the bending of the pedestal caused by temperature gradient
$\Delta z_{truss,g}$	z-displacement due to the bending of the trusses caused by gravity loads
$\Delta z_{tube,bending,g}$	z-displacement due to the bending of the torque tube caused by gravity loads
$\Delta z_{tube,t}$	z-displacement due to the bending of the torque tube caused by temperature gradient
$\Delta z_{tube,torque,g}$	z-displacement due to the twisting of the torque tube caused by gravity loads
ξ	arbitrary number used in definition
φ	twisting angle of the torque tube
α	temperature expansion coefficient of steel
ρ	angle from the center of the heliostat
σ_{aberr}	error due to optical aberrations
ρ_{air}	specific weight of air
σ_{BQ}	beam quality (normal distribution)
$\sigma_{buckling}$	buckling stress
$\sigma_{canting}$	canting error
σ_{grav_loads}	error due to gravity load deformations
σ_{max}	yield stress
σ_{pole}	stress in pole
ρ_{steel}	specific weight of steel
σ_{sun}	optical error due to the sunshape normal distribution
Δt	temperature difference
σ_{temp_loads}	error due to temperature load deformations
σ_{Total}	total beam dispersion error
$\sigma_{waviness}$	error due to facet waviness

1 Introduction

The generation of electricity in solar thermal power plants started in the early seventies with the intention to reduce the dependency on limited fossil primary energy. Several concepts were developed to a turn-key stage and nine parabolic trough plants with a total of more than 350 MWe are operated in California with profit. However, falling oil prices and the lack of political support hindered an entry in the world wide energy market. Recently, the integration of solar thermal power technology in conventional power plants (hybridization) gained importance. A conventional power plant with a solar part can be used in medium- or even base-load operation in order to distribute the solar investment costs among a larger amount of produced electricity. This lowers the financial risk and makes it possible to fulfill the duties of the electricity supplier at every time. The special significance of solar thermal power tower technology (also called central receiver systems) in this domain is underlined by the participation of large industrial companies in respective projects and especially by the realization of such a plant in Barstow, California (Solar Two).

Central receiver power plants use a big number of individually controlled sun tracking mirrors (heliostats) that concentrate the direct solar insolation onto a receiver located on a tower. There the solar energy heats up a transfer medium (molten salt, water/steam, air) which can be used for thermal electricity production in a conventional steam process.

The collector field consists of thousands of heliostats and is a key component of the solar power plant in the technical and economic point of view. At the same time, errors in tracking and low beam quality of the heliostats are the main reasons for energy losses during operation. Therefore a main condition to introduce solar tower power plants in the world-wide energy market is to further improve heliostats and their control and to reduce their specific costs.

To reach this goal, a so called "large-area heliostat" ($>100 \text{ m}^2$) was developed by CIEMAT, the Spanish center of energy and environmental technologies. Large-area heliostats offer lower specific costs because, for a given size collector field, they have fewer drive assemblies, pedestals, foundations, controllers, and structural assemblies. After manufacturing, the heliostat prototype (GM-100) in the classical T-shape was erected and evaluated at the Plataforma Solar de Almería.

During an extensive test program carried out through 1997, it was observed that the reflected beam showed an unforeseen behavior. The GM-100 yields a lower beam quality than expected and the focus spot displays significant distortions during an operation day, especially close to sunrise and sunset.

In the following study, the cost reduction potentials of heliostats and the effect on the energy production costs of solar tower power plants in general will be discussed briefly, then the focus deviations resulting from deviations and temperature changes of the GM-100 will be examined in detail. Various measurement techniques will be employed in order to characterize the actual focus development during an operating day as well as the reasons for the deviations of the focus spot, i.e., the deformations of the support structure and its temperature changes. The essential error sources of heliostats will be inquired generally and a mathematical model of the deformations of the heliostat support structure considering gravity-induced loads and temperature gradients will be developed. With this information, theoretical predictions of the focus development will be made and compared with the measured results.

The purpose is to explain the distortion of the focus and identify the main error contributors. The theoretical simulations yield a mathematical function of the deformation development as a daily and seasonal function of the concentrator elevation angle. This information can be used in several ways to improve heliostat performance. An improved heliostat support structure that will lead to a better beam quality and an additional cost reduction will be planned, built and tested. Moreover, the actual focus deformation can be calculated continually and be integrated in a future tracking system. With this it will be possible to obtain an equal flux distribution over the receiver surface and reduce spillage (amount of energy that does not hit the receiver aperture) and so compensate with comparatively cheap software for hardware errors that are the consequence of low-cost constructions. Additionally, the given theoretical relation between mirror size and beam quality helps to choose the optimal heliostat size.

2 State of the Art in Thermal Solar Power Plant Technology

This chapter gives a brief overview of the different concepts of thermal solar power plants. It shows the present state of the central receiver technology and its components and gives some examples of actual test campaigns on the PSA.

2.1 Overview

The insolation at the outside of the earth's atmosphere has, depending on the sun-earth distance during the year, an average value of $1\,367\text{ W/m}^2$ (solar constant) /WINTER 1991/. Due to atmospheric losses, a good site on the ground gets about $1\,000\text{ W/m}^2$ of direct radiation. This results in a huge total amount of energy that arrives on earth's surface every day, however, with a low energy density. Therefore, all solar thermal systems for electricity generation use the concentration of sunlight to obtain the high temperatures required for an efficient thermodynamic cycle /CIEMAT 1996/.

The three main concepts of solar energy concentration originate from the ideal design for uniform radiation collection, the parabolic dish (Fig. 2-1, a). Consequently, the highest concentrations are available from such devices. However, unit size is limited to diameters of 10 to 20 m because of aberration due to deviation from the ideal shape and innate construction defects. This implies that a power station with parabolic dishes would have to consist of many, e.g., 25 kW (approx. 12 m diameter) units, each delivering electricity. Because of the high concentration, temperatures above $1\,000\text{ }^\circ\text{C}$ can be attained. An important cost reduction with size (25 kW x 1 000 units = 25 MW) cannot be expected, except in as much as all would use the same infrastructure, facilities and personnel. Otherwise, the concept's modularity makes it ideal for small, stand-alone applications /CIEMAT 1996/.

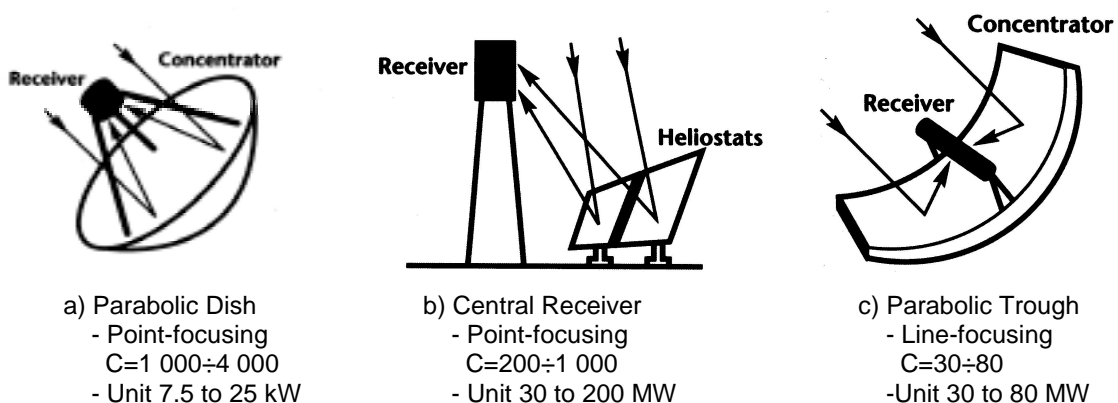


Fig. 2-1: The three concepts of concentrating solar thermal electricity generation

The central receiver concept is the parabolic ideal carried to a larger scale (Fig. 2-1, b). This concept uses parts of several parabolas that are represented by various heliostats. The multiple rows of heliostats with different focal lengths belong to several fictitious parabolas (Fresnel approximation). The advantage of this concept is that the solar energy is collected in the original radiative phase, permitting units of up to 200 MW_e . The limit is determined by the efficiency of

the farthest heliostats in the transfer of solar radiation to the top of the tower. Concentration is possible up to around a thousand suns (1 sun = 1 kW/m²), which corresponds to temperatures up to 1 000 °C.

The parabolic trough concept (Fig. 2-1, c), represents the greatest simplification, since it differs even more from the ideal parabolic form. The curvature conforms to the ideal only in one dimension, its cross section that extends linearly down an open semi-cylinder. This results in a linear focus capable of clearly lower concentration and temperatures of 200 to 400 °C, also limited by the temperature range of the oil used as heat transfer fluids. This concept is well suited to modularization, collecting the energy in many parallel rows. Therefore, as well as due to its simplicity, this was the first of the concepts to be used in a solar thermal power plant. In California, these plants feed a total of more than 350 MW_e to the grid. Unit size goes from 15 MW_e to 30 MW_e and up to 80 MW_e with a reasonable limit of 200 MW_e/CIEMAT 1996/.

The following paragraphs are focused on central receiver systems, which is the technology that uses heliostats.

2.2 Solar Tower Power Plants (Central Receiver Systems)

Table 2-1 shows the existing central receiver test facilities and pilot plants world-wide. They all consist of a concentrator (heliostat field), a receiver and a conventional steam cycle as described above, but they differ in field size and the receiver principle. The solar components will be described in more detail.

Table 2-1: Test Facilities and Pilot plants 1997

Facility	Principle	Power	Location	Status
CESA-I	Water/Steam Tube Receiver	1 MW _{el} (9 MW _{th})	Almería (Spain)	1983-84 in operation, now test facility for several concepts (e.g. GAST, TSA, REFOS)
Eurelios	Water/Steam	1 MW _{el}	Adrano (Italy)	In operation '81-'84
GAST	Air Tube Receiver		Almería (Spain)	deactivated
Phoebus	Open Volumetric Air Receiver	30 MW _{el}		Turn-key offer
Sandia National Solar Thermal Test Facility	Test Facility for Central Receivers	5 MW _{th}	Albuquerque, NM (USA)	Test facility
Solar One	Water/Steam Tube Receiver	10 MW _{el}	Barstow, CA (USA)	1982-88 in operation transformed to Solar Two
Solar Two	Salt / Tube Receiver	10 MW _{el}	Barstow, CA (USA)	in operation since 1996
SSPS	Na- Tube Receiver, since 1987 Volumetric Air Receiver	0.5 MW _{el}	Almería (Spain)	Since September 1981 testing of systems and components
Themis	Salt Receiver	2.4 MW _{el}	Targassone (France)	in operation '83-'86, test facility
TSA	Open Volumetric Air Receiver	3 MW _{th}	Almería (Spain), CESA-I -Tower	In operation since 1993
Weizmann Institute of Science	Test Facility for solar thermal and chemical applications	3 MW _{th}	Rehovot (Israel)	Test facility

2.2.1 Heliostat Field

The purpose of the heliostat field is to reflect the maximum amount of sunlight, as evenly distributed as possible, into the receiver aperture. It consists of a large amount of heliostats (up to several thousand) that are situated either around or in a circular sector in front of the tower. All heliostats consist of a concentrator, a support structure, azimuth and elevation drives, foundation and a control unit. In order to reflect the sunlight to a specific point in space, they need to follow the sun in two axes (tracking). The respective elevation and azimuth angles for every heliostat are either calculated by a local computer or a central computer that sends them in intervals of a few seconds to the heliostats.

The main tasks of heliostats are:

- aim exactly at the receiver aperture (tracking)
- keep the beam well focused (beam quality)
- high reflectivity

Both, tracking accuracy and beam quality determine the amount of spillage, i.e., the amount of energy that does not hit the receiver aperture. Presently, there are mainly two different design principles: faceted glass/metal heliostats and stretched membrane heliostats (see Fig. 2-2).

Faceted glass/metal heliostats. This conventional type of heliostat has a concentrator consisting of many rectangular mirrors (facets) with a size of usually about $2\div 3\text{ m}^2$ (cf. Fig. 2-2, left). The facets are mounted on trusses that are connected to a torque tube. They are curved to the respective focal length and canted (adjusting the facets on the support structure to form the parabolic shape) so that their pictures add up at the same focus point. The drives that move the torque tube in two axes are mounted in a gear box on top of a vertical steel tube, the pedestal. Heliostats of this type are also called T-shaped heliostats, because their support structure is in the form of the letter ‘T’.

Stretched membrane heliostats. Instead of the conventional structure with many facets, this type of heliostat usually has a single facet design (there exist also some mixed designs that have several small membranes mounted on a T-shaped support structure). The concentrator consists of two metal membranes that are attached on the front and back side of a metal ring. The front side is covered with thin glass mirrors to obtain the desired reflectivity. A vacuum in the inside deforms the membranes and creates a parabolic concentrator with adjustable focal length. This eliminates the canting procedure. The membrane can be mounted on a pedestal as described above or be supported by a steel framework like the ASM-150 (cf. Fig. 2-2 right).

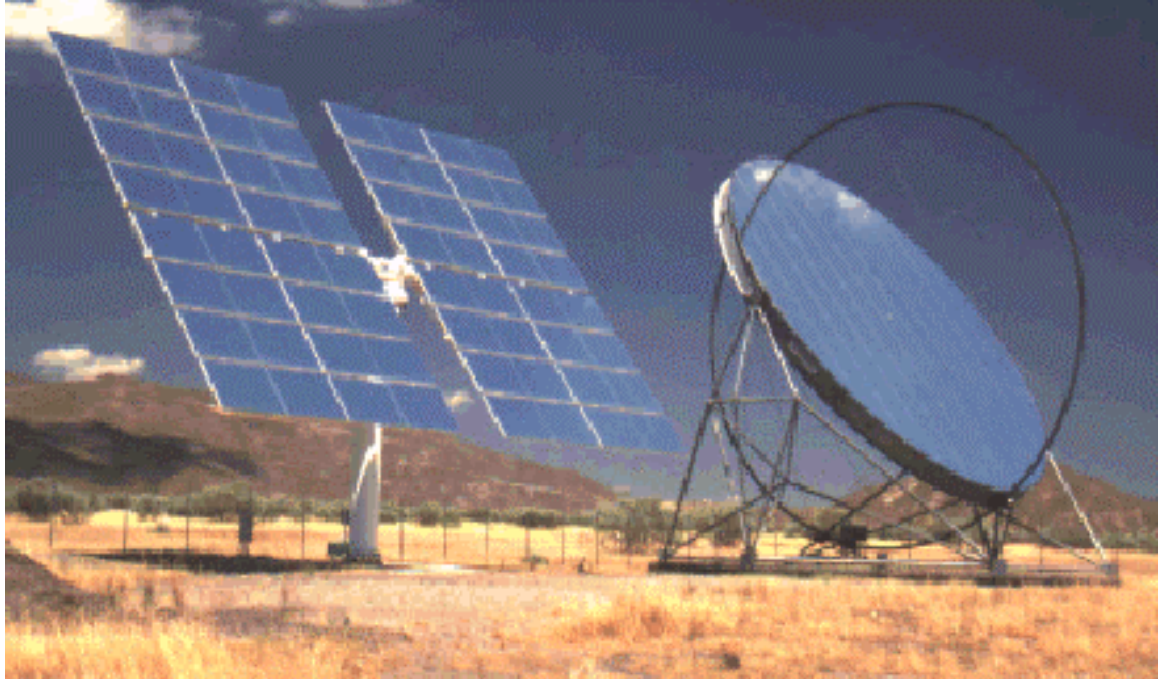


Fig. 2-2: The two large area heliostats tested at the PSA: GM-100 (left), ASM-150 (right)

2.2.2 Receivers

The receiver absorbs the incoming radiation and passes it on to a heat carrier (water/steam, air, molten salt, sodium). Depending on the concentration factor and the heat transfer medium, different receiver designs were developed and tested in the past (see Table 2-1).

Tube receivers. Tube receivers consist of a tubular heat exchanger, in which the absorption occurs at the tube surface. The American plant "Solar Two", for example, uses a tube receiver with molten salt.

Volumetric receivers. PHOEBUS by contrast has a volumetric receiver that is constructed as a knitted wire mesh. The solar radiation can penetrate into the mesh and is mainly absorbed and transformed into heat by the wires deeper within the absorber. A fan sucks air through the wire mesh. The airflow takes up the heat and the wires at the front of the receiver are cooled by the incoming cold air. The surface temperature is lower than the maximum air temperature and therefore the back-radiation losses are minimized.

An essential design feature of the absorber is its modular construction. It consists of hexagonal modules of identical size that can be easily exchanged and allow receivers to be built in practically any size. Air as the heat carrier is non-polluting, non-corrosive, non-inflammable, universally available and easy to handle.

Since 1993 a test circuit with the air receiver and thermal storage with a capacity of 3 MWh (TSA, Technology Program Solar Air Receiver) has been on test in the European Solar Research Center in Almería. The test results are excellent /SCHMITZ-GOEB 1996/.

Pressurized volumetric receivers. A significant improvement of system performance can be obtained with pressurized volumetric receivers because the hot air can be directly fed to a gas turbine in a combined cycle plant with a much higher efficiency. This is the goal of the REFOS project, which is presently tested at the PSA. The system is supposed to work with a pressure of 15 bar and temperatures between 400 and 800 °C. It consists of several hexagonal modules that can be combined to the desired size. They consist of a secondary concentrator (funnel-like mirror arrangement) and a volumetric receiver that is sealed by a quartz window to hold the pressure /PITZ-PAAL 1997//REFOS 1998/.

2.2.3 The PHOEBUS Concept

Since in the present fossil energy price situation solar power plants are not yet economic, the integration of central receiver systems in conventional power plants (hybridization) is a promising step to introduce this technology as fuel saver in the energy market of the sun-belt states. A conventional power plant with a solar part can be used in medium- or even base-load operation in order to distribute the solar investment costs among a larger amount of produced electricity. This lowers the financial risk and makes it possible to fulfill the conditions of the power purchase agreement.

For this purpose the PHOEBUS power plant, a hybrid system with a capacity of 30 MW_{th} offered on a turn-key basis, was developed. It consists essentially of two different parts: the conventional power plant and the solar part consisting of concentrator (heliostat field) and receiver. This concept uses ambient air as heat transfer medium. A so called volumetric receiver, that differs significantly from the tube absorbing systems of other concepts (see chapter 2.2.2), absorbs the incoming concentrated radiation and passes the energy on to the air. The air leaves the receiver with a temperature of 700 °C (Fig. 2-3) and flows through a steam generator that creates the high pressure steam necessary to run the turbine. When the solar input is not sufficient, a duct burner fired with gas between the receiver and the steam generator can produce additional heat. Hence, the solar tower power plant can always produce electricity, even during periods of insufficient insolation and in the night /PITZ-PAAL 1997/.

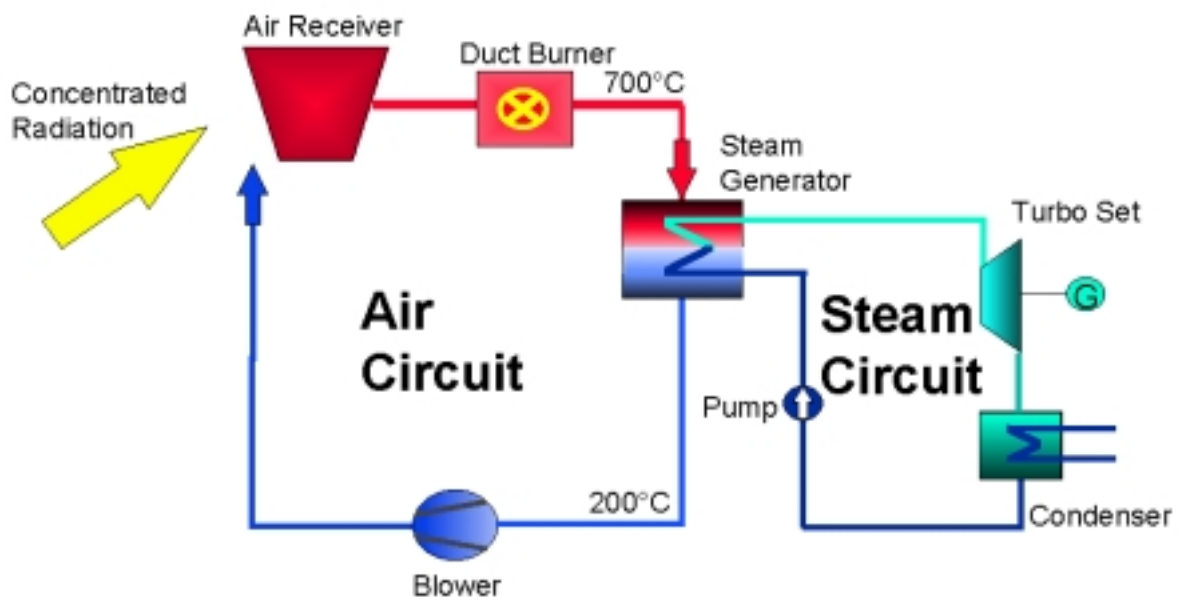


Fig. 2-3: Principle of the PHOEBUS solar power plant /STEINMÜLLER 1995/

3 Costs and Potential of Cost Reduction

The environmental attractiveness and technical feasibility of tower SPPs (Solar Power Plants) was already described in other papers /WEINREBE 1998/. However, to compete with conventional technologies in the energy market it is essential to have comparable or lower energy production costs. This chapter gives an overview of investment costs, energy production costs and potentials of further cost reduction. Especially the costs of heliostats, their further cost reduction and the consequences are considered.

3.1 Solar Tower Power Plants

The total investment cost of a tower SPP is considerably higher than that of a comparable conventional plant and depends, besides of the plant size, mainly on the solar multiple (SM, i.e., the ratio of the input absorbed at the input end, to the fraction of input required to deliver rated output at the output end /WINTER 1991/), the storage capacity and the receiver technology. Table 3-1 demonstrates the capital cost of various concepts.

Table 3-1: Cost Estimates for Second Generation Towers /BECKER 1993/

Second Generation Central Receiver Technology	Capital Cost (\$M)
30 MWe, Salt, Solar-Only SM=1.4, 4.5h Storage	95.3
30 MWe, Salt, Hybrid 25 % SM=1.4, 4.5h Storage	99.5
30 MWe, Air, Solar-Only SM=1.2, 3h Storage	99.4
30 MWe, Air, Hybrid 25 % SM=1.2, 3h Storage	101.3
100 MWe Salt, Solar-Only SM=1.6, 7h Storage	222.7
100 MWe Air, Only Solar SM=1.8, 8h Storage	272.7

The largest single contributor to total tower SPP investment cost even for a future estimation with optimistically reduced collector costs is the cost for the heliostat field (Fig. 3-1). At the beginning of tower SPP development fifteen years ago, the heliostat field cost share could have been 50 % or more of total cost (for a plant without storage). As a result of technological advances in heliostat technology, this share could be already lowered. Because economy-of-scale effects decrease the specific cost (\$/kWe) of power conversion subsystem, the cost share of the heliostat field and heliostat foundations increase with SPP size (assuming SM=1.0). The inclusion of thermal storage necessitates a SM > 1.0, requiring more heliostats and leading to correspondingly higher heliostat field/foundation cost shares quite independent of plant rating. Hence, the percentage of heliostat subsystem costs is to be viewed in conjunction with plant rating and SM /WINTER 1991/.

Fig. 3-1 also shows that the cost of the receiver/tower subsystem is merely about 12 % of total investment, dependent on SPP rating and SM. The key factors influencing receiver/tower costs are heat transfer medium, temperature and pressure, receiver size and configuration, whereas the impact of volume manufacture is only minor. A storage system of 7 hours capacity represents

10 % of total investment, but depends strongly on capacity factor (CF, i.e. energy produced over specified time period(s), divided by the product of nameplate power rating times the aggregate hours of the time period(s) chosen /WINTER 1991/) and storage medium. The conventional turbine cycle requires about 15 % of the total cost. The item *others*, with 33 % of the investment cost, comprises all indirect costs such as construction management, equipment rental, spares, land and infrastructure, impact studies, etc.

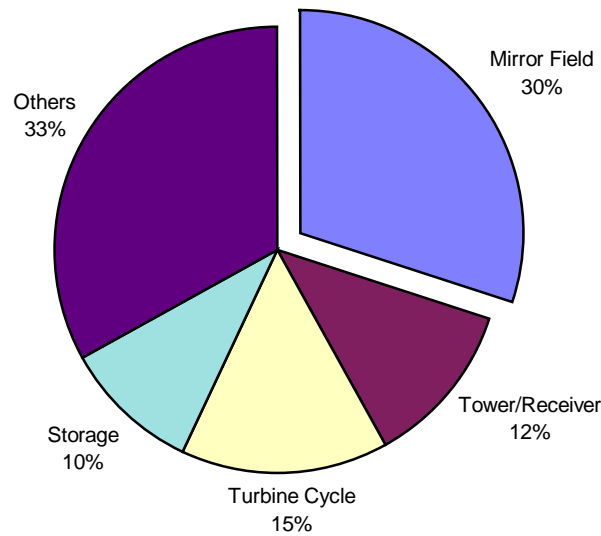


Fig. 3-1: Estimated Future Investment Cost Structure of a 100 MW Tower SPP with 7h Storage /WINTER 1991/

All this shows that the collector subsystem is not only the largest single cost element of a central receiver plant, but also the one with the highest potential of cost reduction. The conventional parts like power block, tower and all the components summarized under *others* have little cost reduction potential. Only the solar components heliostats, receiver and possibly the storage system can become notably cheaper. Fig. 3-2 shows the sensitivity of the LEC (levelized electricity cost, i.e. the constant annual revenue per unit of energy required over the lifetime of a plant to compensate for its fixed and variable costs, interest costs and shareholder return /WINTER 1991/) on various parameters. The biggest influence on solar LEC has the interest rate, however, this cannot be controlled by engineering. The most important factor that can be influenced is the heliostat cost which affects the solar thermal output by almost 2 cents per kWh considering the present uncertainties on heliostat costs (ranging from 100 to 240 \$/m²) /SÁNCHEZ 1996/. Very optimistic long-term development goals aimed even at 40÷80 \$/m² /WINTER 1991/ but presently these goals seem unrealistic. Furthermore it can be seen that solar LEC results much less sensitive to variations of the receiver cost.

The study of Johansson shows that the range of solar LEC of a 100 MWe tower SPP is at the moment 8÷16.1 cents/kWh. The projection for a 200 MWe plant in 2010 with technical improvements, large thermal storage and heliostat cost of 75 \$/m² gives an estimated solar LEC of

4.6÷6.5 cents/kWh /JOHANSSON 1993/. Due to a US Department of Energy study, the advanced technologies coupled with economies-of-scale emerging from continued expansion into high-value markets will allow concentrating solar power (CSP) systems to compete in large-scale distributed and dispatchable markets priced at 4 to 6 cents/kWh /BURCH 1998/.

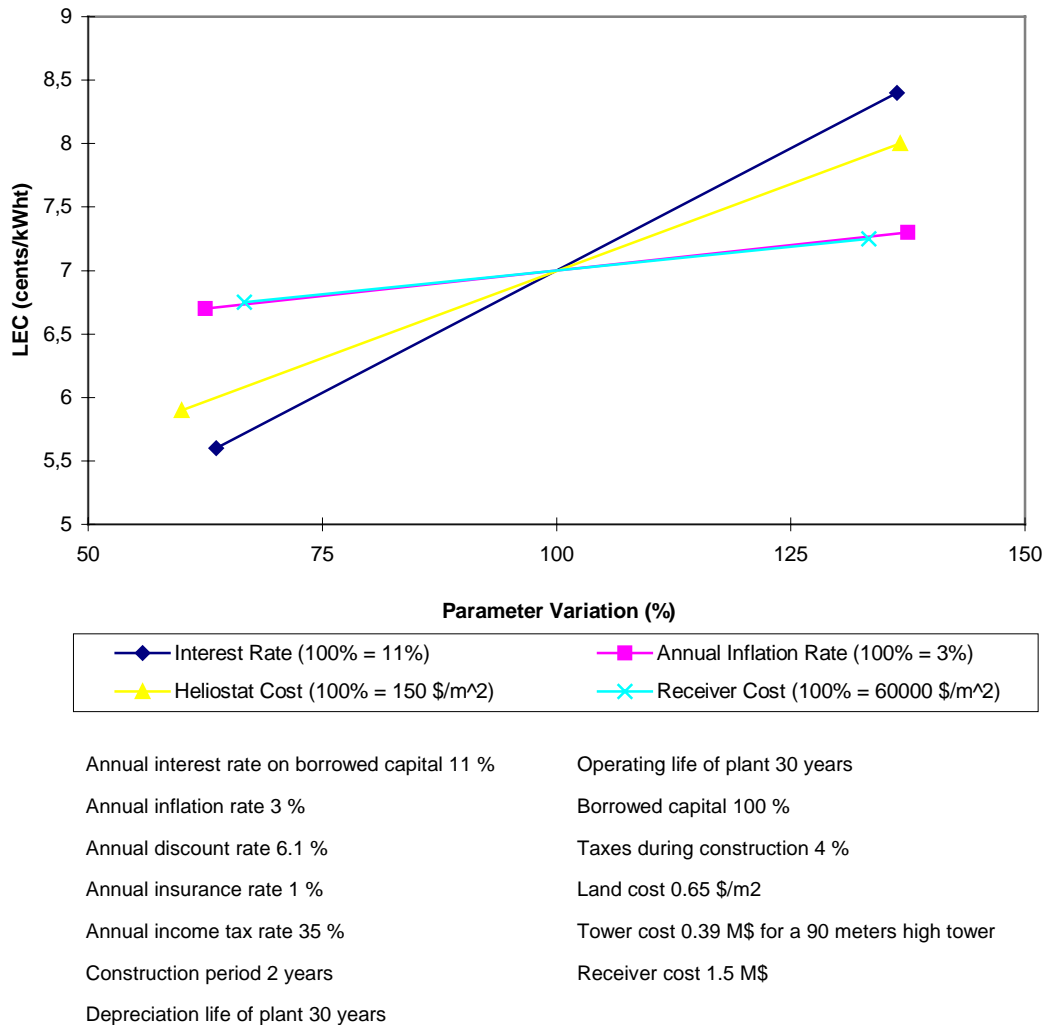


Fig. 3-2: Sensitivity Analysis of the LEC on various Parameters /SÁNCHEZ 1996/

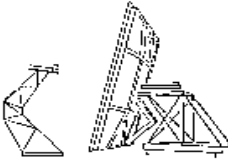
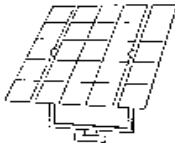
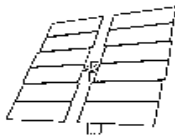
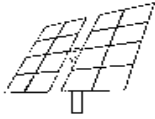
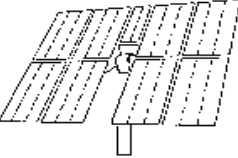
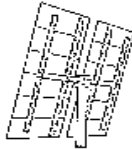
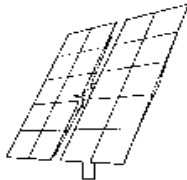
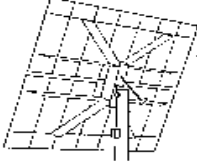
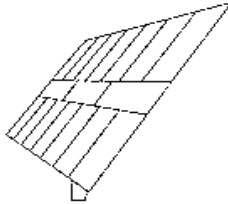
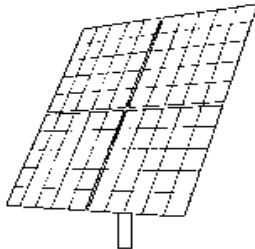
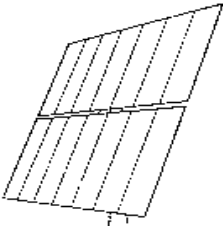
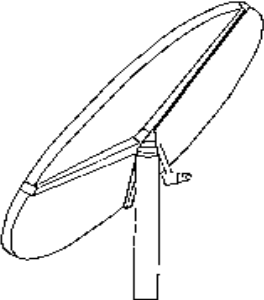
3.2 Heliostats

This chapter gives an overview of heliostat development and specific cost development in the last years and estimated potentials of future improvements. The possible consequences of cost reduction measures on the optical quality will be shown and the notion of beam quality will be explained.

3.2.1 Development and Potential of Cost Reduction

The greatest current driver of the LEC for dispatchable solar power is the cost of solar components as seen above. The purchase price of solar concentrators in the present situation (not for a future power plant as earlier) alone constitutes 40 to 50 % of the LEC of the plant /BURCH 1998/. Therefore, significant effort has been devoted to lowering the cost of heliostats and to estimating their mass-production costs. All the test facilities and pilot plants so far have used glass/metal heliostats that consist of silvered-glass mirrors on steel support structures (GM-100 type). By progressively increasing heliostat size, reducing their structure and improving drives and control, their cost has been reduced from 1000 \$/m² for CRTF heliostats to less than 200 \$/m² today for a large onetime buy. Large-area heliostats offer lower specific costs because, for a given size collector field, they have fewer drive assemblies, pedestals, foundations, controllers, and structural assemblies. In addition they cost less to operate and maintain Studienarbeit, Universität Stuttgart, IER Band 272, Juni '97 /FALCONE 1986/.

Fig. 3-3 shows examples of heliostat development and future trends with their respective specific weight and specific costs. The development goes from early rigid and heavy constructions to lightweight low-cost constructions. Presently, two development lines are followed towards low-cost solutions, (a) the large-area glass-faceted configuration (e.g. GM-100), and (b) the so-called stretched membrane design (e.g. ASM-150). Prototypes of these heliostats are being tested for performance at the PSA test site, but it is not yet obvious which design is the better one. The large-area glass/metal prototypes in Spain and in the United States showed a poor beam quality /MONTERREAL 1996//STRACHAN 1993/ which to examine is the subject of this study, however, they bring a large amount of operational experience, have a simple structure and showed a good reliability (>96 %) during Solar One operation. Estimates promise a future cost goal of 60÷80 \$/m² for glass/metal heliostats. The stretched membrane designs are rather new and are said to have the potential to become as cheap as 40÷60 \$/m² /WINTER 1991/. Their optical quality even with large areas is better, however, they exhibit problems with keeping the desired membrane shape in sudden wind gusts /GLAHN 1998/, are more difficult to mount on-site and have by far less operational experience.

Weight* (kg/m ²)	Glass-metal technology	Price/cost** (\$/m ²)
a 100		a 4000
b 76		b 900
c 54		c 400
d 51		d 800
e 69		e
f 50		f 1000
g 56		g 250
h 47		h -220-120***
i 43		i 180-100***
k 39		k 150-80***
Silver-polymer / silver-steel technology		
l 35-25***		l 120-60***
m 20***		m 80-40***

* w/o foundation

** 1987 basis

*** estimate/goal for volume production

Fig. 3-3: Status and Trends in Heliostat Development: Technology, Configuration, Specific Weight and Specific Costs /WINTER 1991/

There are several ways to reduce the heliostat costs. One is to further develop the stretched membrane technology and gain operational experience, the other is to improve the poor optical quality of large-area glass/metal facet heliostats and further reduce their specific costs.

The estimated prices of installed second generation faceted glass/metal heliostats can be broken down in the following manner /MAVIS 1989/:

- 75 % for reflective assembly, drive mechanism, and support structure
- 12 % for controls and field wiring
- 13 % for foundation/pedestal

The reflective assembly, drive mechanism, and support structure costs incurred at the central manufacturing facility can be subdivided further:

- 63 % for direct materials costs
- 9 % for fully loaded direct labor costs
- 5 % for capital replacement costs
- 6 % for gross profit
- 17 % for consumables, indirect expenditures, general and administrative costs, property tax and insurance, transportation to the site, and other expenses

Unfortunately, the cost of the single parts of the GM-100 are not available. Nevertheless, based on the numbers given above, some general considerations can be made. The costs of single parts (foundation, support structure, drive unit and control unit) can be distributed to a larger area by going to a large unit size, this way the specific costs are reduced. It can be seen that the costs for the reflective assembly, drive mechanism, and support structure consist mainly of direct material costs (63 %), therefore the material reduction of the facets, the drive units and above all of the weighty support structure inhibits the highest cost reduction potential.

3.2.2 Consequences of Cost Reduction Measures on Beam Quality

Reducing the specific costs of a heliostat by simplifying its support structure, by reducing its weight and by going to a larger unit size usually has a contradictory effect on the beam quality. Increasing pointing error or beam quality errors of the whole field of heliostats is not cost effective /MARTIN MARIETTA 1982/. In order to judge and improve the optical quality of a heliostat, it is necessary to know the error sources and have a merit number to quantify it.

Error sources. Three different types of error sources contribute to the final focus shape a position. First, the sun is not an ideal point light source. Second, the real concentrator shape slightly differs from the ideal shape, this makes the focus to distort and widen (slope error). And third, the concentrator normal may differ from the assumed normal, this makes the heliostat to reflect to a different point (tracking error).

The best result that can be obtained from a reflective concentrator is an exact picture of the sun itself, however, the sun is not an ideal point light source. The probability density function describing the distribution with respect to the central ray from the sun is called *sunshape*. This directional distribution is widened by atmospheric scattering, especially during hazy atmospheric conditions. Light clouds can cause considerable broadening of the sunshape. The size of the solar disc is about 2.3 mrad (standard deviation) without atmospheric scattering but can reach much higher values /HELIOS 1979/.

When a light ray undergoes a specular reflection from a concentrator surface, the angle of reflection is equal to the angle of incidence (Snell's Law) /HELIOS 1979/. These angles are measured with respect to the surface normal at the point of reflection. However, in solar-collector applications, the direction of the surface normal is not always exactly known. The surface normal at a given place on the facet deviates from its design value because of waviness of the facet surface, orientation errors from canting and because of structural deformations due to gravity loading, temperature and wind influences. These deviations cause the reflected rays to spread around the central ray (slope error) or, in case the whole concentrator has a wrong orientation, they make the central ray to be reflected to a different point (tracking error).

Quantification. The irradiance distribution of the reflected rays can be mathematically characterized by the standard deviation of the reflected rays from the central ray. This can be done with the coordinates of the points of the reflected rays on a reference target perpendicular to the reflected rays:

$$\rho_x = \sqrt{\frac{\sum I_i (x_g - x_i)^2}{\sum I_i}}, \quad \rho_y = \sqrt{\frac{\sum I_i (y_g - y_i)^2}{\sum I_i}},$$

where (3-1)

$$x_g = \frac{\sum I_i x_i}{\sum I_i}, \quad y_g = \frac{\sum I_i y_i}{\sum I_i},$$

are the coordinates of the beam centroid /MONTERREAL 1997/. The units of ρ , initially longitudes from centroid, are converted into angular units (subtended angle by ρ from the center of the heliostat in mrad) in order to make the characterization of $I(x,y)$ independent of the plane where it was projected by the heliostat. ρ is usually called the *total beam dispersion error* and will be represented by the Greek letter σ_{Total} .

Taking into account that the so-called image constituents, *i.e.* sunshape, astigmatic aberration, waviness, gravity loads influence, etc., can be assumed to be statistically independent /HELIOS 1979/, the total beam dispersion error of the distribution is:

$$\sigma_{Total}^2 = \sigma_{sun}^2 + \sigma_{aberr}^2 + \sigma_{BQ}^2 \quad (3-2)$$

where σ_{sun} is the error due to the sunshape, σ_{aberr} is the error due to optical aberrations and σ_{BQ} is called the *Beam Quality* of the heliostat /MONTERREAL 1997/. In the PHOEBUS project, the required beam quality value is 2.6 mrad under design conditions (see Table 4-1).

The contribution of the optic errors to the dispersion of the reflected beam can also be expressed in its own individual effects /WINTER 1991/:

$$\sigma_{BQ}^2 = \sigma_{waviness}^2 + \sigma_{canting}^2 + \sigma_{grav_loads}^2 + \sigma_{temp_loads}^2 + \dots \quad (3-3)$$

The value for the optical quality for usual facets (waviness) is in the range of 1.5 mrad. Values for the canting error depend on the methodology and are not exactly known /MONTERREAL 1998/. The deterioration of the beam quality due to gravity loads and temperature influences will be determined in this study. The deflection of the ideal concentrator surface at a specific point lets the incoming ray wrongly reflect twice the angle of the deviant surface normal. Introducing the resulting deviations of the x- and y-coordinates of the points on the target in equation 3-1 leads to the slope error of the heliostat due to structural deformations. The relation of the deformations at the outer ends with the slope error will be determined once and any further values will be obtained using a proportional factor.

4 The GM-100 Glass-Mirror Heliostat

This chapter gives an overview of the GM-100 heliostat, its features and its structural design. The observed performance and beam quality of the 1997 test program is described. Based on this, an analysis of the present problems and a specification of the possible causes is made. In order to clarify the performed calculations of the structural deformations, the mathematical model and the derivation of the formulas are described in detail.

4.1 General Description

CIEMAT has developed this large area heliostat with the purpose of reducing the costs by going to a larger unit size, reducing the weight and simplifying fabrication and mounting .

The net heliostat reflecting area (105 m^2) is composed of 32 newly designed facets (Fig. 4-1). The mirror facets of the heliostat are mounted on a rack forming two separate mirror panels. The facets of each panel are supported by four welded trusses of 9 m length. The two panels are mounted on the heliostats' 12.4 m long, 0.4 m diameter torque tube. The whole reflector assembly is bolted to the central drive unit situated on a 4 m high, 0.61 m diameter pedestal. The foundation is made of a 13 m^3 concrete block. Further technical specifications of the heliostat are given in Table 4-1.

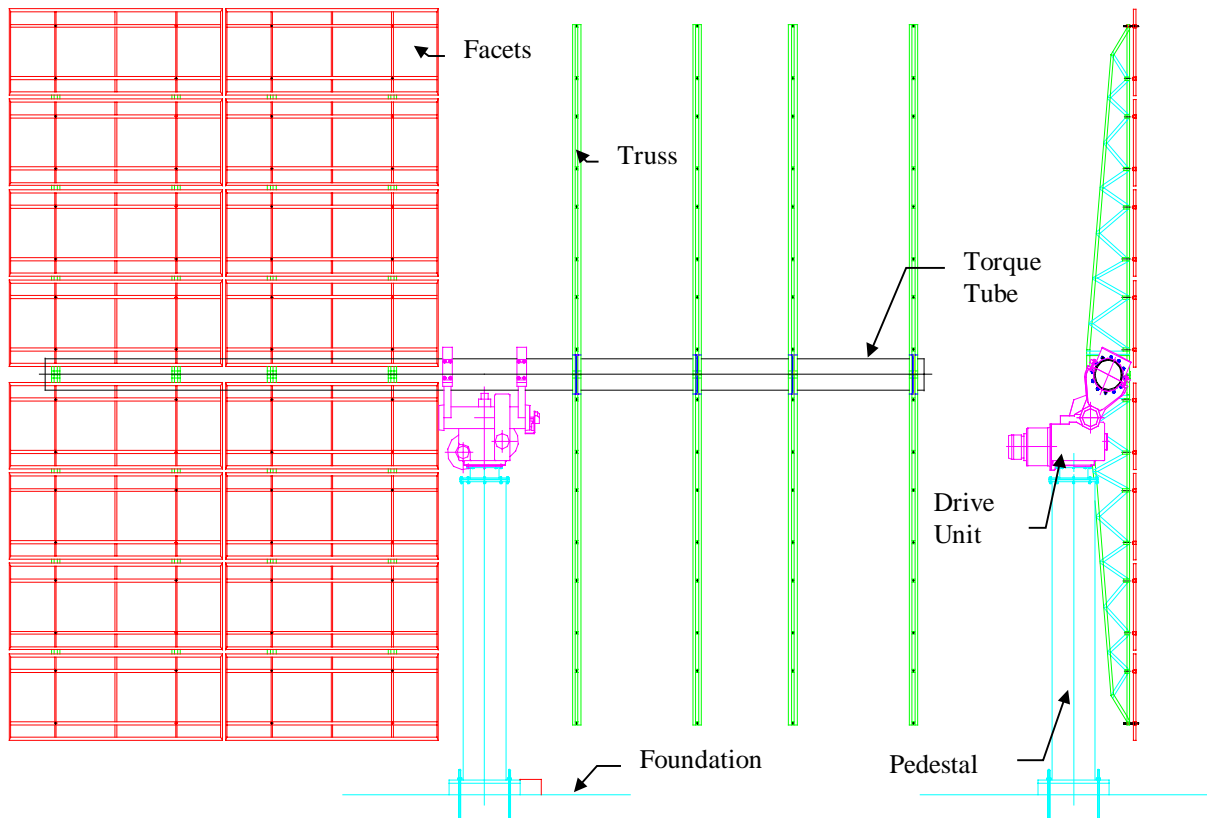


Fig. 4-1: Front and lateral views of GM-100 heliostat.

The unit was manufactured by the Spanish company JUPASA and installed at the PSA during the first half of 1996. A focal length of 480 m was established and its performance was tested with the help of the PSA HERMES camera flux measurement system.

Table 4-1: Characteristics of the GM-100

Concentrator	
Concentrator concept	glass/metal facets
Reflective surface	glass mirrors: 32 facets of 1.1x3 m.
Focal length	480 m.
Area	105 m ²
Desired beam quality	<2.6 mrad for wind speeds up to 40 km/h
Specific facet weight	17 kg/m ²
Tracking unit	
Axis	azimuth/elevation
Support structure	T-shape
Start-up/shutdown time	15 minutes
Stow position	face down (-90° ± 5°)
Desired tracking quality	0.9 mrad elevation/0.2 mrad azimuth
System control	
Heliostat control system	Theoretical calculation of sun position
Data acquisition system	None
Instrumentation	endlimit switches, encoders
Limits	
Survival (in stow position)	wind speeds up to 140 km/h
Normal operation	wind speeds up to 40 km/h
Reduced operation	wind speeds between 40-60 km/h
Ambient temperature	-10 ≤ T ≤ 50 °C
Hailstones	20 mm at max. impact velocity 20 m/s in any direction
Seismic activity	0.6 m/s ² horizontal dynamic acceleration
Lifetime	30 years for all components

4.2 Performance and Beam Quality

The GM-100 was canted at spring equinox at solar noon, this means that at this time and elevation the concentrator facets were adjusted to form the desired parabolic shape. Four months later, the focus at noon (now at a higher elevation) showed significant distortions (Fig. 4-2a). Taking into account that there are two relatively well conformed and overlapping focuses on the target, it can be deduced that both right and left branches of the heliostat keep their facets grouped, but the probable backwards bending of the horizontal torque tube makes their focuses diverge. This assumption was supported by the CCD camera located in the eastern focus, which shows that the corresponding eastern branch of the heliostat is illuminated (Fig. 4-2b).

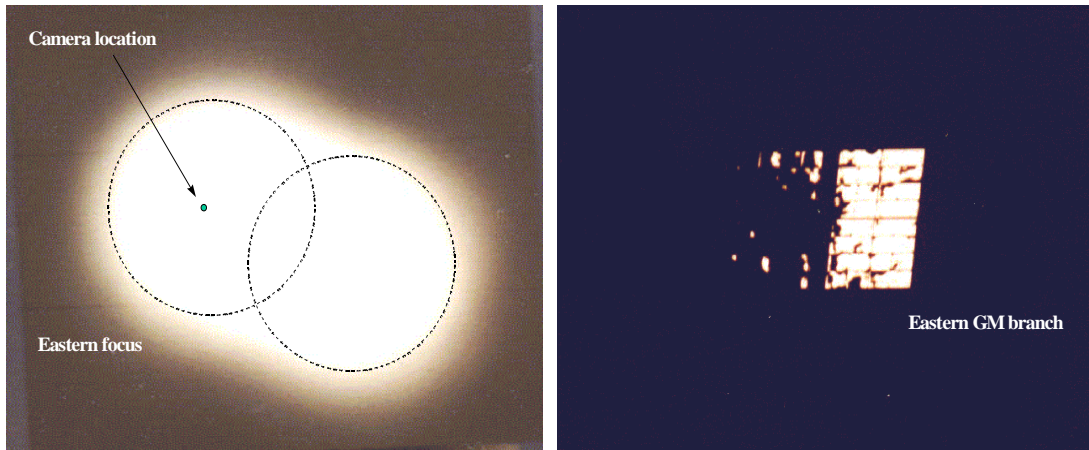


Fig. 4-2a and b: GM-100 split focus at noon, 4 months later from canting point

The heliostat performance at sun-rise and sun-set (very small elevation angles) was also altered by a similar phenomenon. Fig. 4-3a shows the appearance of the focus early in the morning. Again the reasonable assumption that the torque tube bends in the direction opposite (forward) that it does at noon was validated by the CCD camera in the eastern heliostat focus, which shows that the western branch of the heliostat is illuminated to the contrary (Fig. 4-3b). This indicates the divergence of the two concentrated beams coming from the both eastern and western heliostat branches with their facets well grouped /MONTERREAL 1997/.

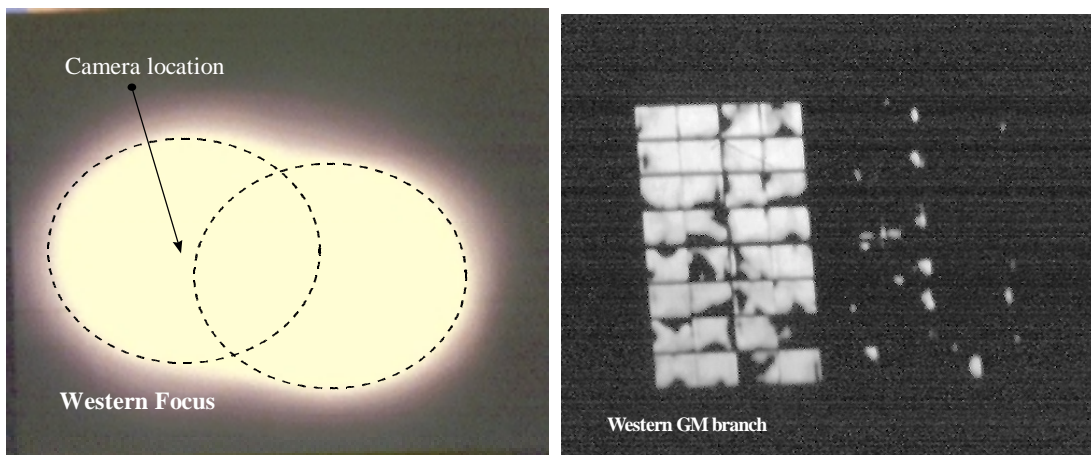


Fig. 4-3a and b: GM-100 split focus early in the morning

The two focuses are not only split up horizontally, but also shifted vertically. To improve the performance of the GM-100 during the summer months, the heliostat was recanted July, 18th, 1997 at solar noon (74.3°, close to highest sun elevation possible).

Identical focus problems were observed in the large area heliostat testing program of the US Department of Energy. Two faceted glass/metal heliostats of 150 m² (ATS) and 200 m² (SPECO) were built and tested at Sandia National Laboratories in 1993. The similar splitting up in two focus spots at off-noon hours was blamed to gravity-induced structural deflections but never examined in detail /STRACHAN 1993/. The 97.5 m² dual-element stretched-membrane heliostat with

a torque tube assembly built and tested at Sandia National Laboratories exhibits the same behavior even more extreme /STRACHAN 1994/.

Therefore, based on the given data and observations an in-depth revision of the GM heliostat was performed to clarify the reason for this unexpected heliostat behavior /MONTERREAL 1997/.

4.3 Reasons for and Influences on Observed Performance

The problem of the split focus described above may have different causes. Possible error-sources that may significantly influence the focus shape and position will be considered thoroughly. With the knowledge of the observed focus distortions from the flux measurement images and the photographs of the reflecting areas taken from within the focus as shown above, the important influences can be identified, examined closer and those without significant effect can be neglected.

Focus distortions are caused by deformations of the ideal mirror shape and by optical aberrations as described in chapter 3.2.2. All the inaccuracies that lead to a stochastic distribution of the reflected ray (waviness of the facets, inaccurate facet shapes, canting inaccuracies, fluctuating wind loads, play in drives etc.) cause the focus to blur or smear, but are not the reason for the deformation of the focus shape. Calculations of the optical aberrations showed that they indeed cause a slightly slant and oval focus spot when the rays come in far off-axis, but by far less than observed. Therefore the explanation for the split focus must be in the deformation of the support structure.

4.3.1 Exterior Influences

The acting exterior influences and their consequences on the structural parts are analyzed separately in the following paragraphs.

Gravity loads. Gravity always leads to bending of the support structure due to its weight and the weight of the facets. It is the main task of the construction to minimize this effect with properly dimensioned structural parts. This is often contradictory to keeping it cost-efficient, lightweight and simple. The new heliostat prototype has still the conventional design, but uses less material for the support structure and is much larger than earlier ones, which means it must bear higher stresses and hence larger deformations. This considerably effects its performance.

Temperature. The changing ambient temperature has only an effect on the temperature of the heliostat as a whole. There are no constructional constraints, therefore the whole structure will increase or decrease in size, but not bend out of shape. However, the radiation of the sun will heat up all parts facing the sun while all other parts in the shade stay cooler. The resulting temperature gradient causes bending and must be considered in the affected structural elements.

Wind loads. Static and dynamic wind loads have an effect on the position and shape of the concentrator. However, the observed behavior occurred every day, with or without wind, therefore this cannot be the reason for the measured effects, only for additional distortions. To get at least an impression of the scale of wind effects, a simple estimation of the consequence of a static, frontal (normal to the concentrator surface) wind load will be calculated. Dynamic wind loads

cause dynamic movements of the heliostat that are not feasible to be calculated with the given tools. Since this is a statistical effect that cannot be eliminated with an intelligent control, the only possibility to minimize the oscillations is by improving design and the rigidity of the construction.

4.3.2 Effects on Structural Parts

Foundation. The 13 m³ concrete foundation is oversized in order to surely avoid any movement or errors due to an unstable basement. Therefore it can be considered as a completely rigid base.

Pedestal. The pedestal consists of a steel tube. The whole concentrator is eccentrically mounted on its top (cf. Fig. 4-5) and hence generates a moment due to gravity loads that changes with the angle of elevation. This bends the pedestal and with it the complete concentrator forward at low elevation angles. Additionally, the spatial temperature gradient due to the direct radiation causes the expansion of the tube on the side facing the sun. This results in a backward bending of the pedestal and the mirror plane with raising temperature differences. Both effects add up during the middle of the day and cause the central focus spot to move up vertically. They do not alter its shape though, therefore this is just relevant for a correction of the tracking.

Torque tube. The torque tube consists of a steel tube as well. Considering the problem of the split focus and regarding the images of the reflecting facets taken from within the focus, it becomes evident that the main reason for this behavior is the bending of the torque tube. The magnitude of the bending due to gravity loads is dependent on the elevation angle and causes the two panels to tilt away from each other at higher elevation angles. This lets them reflect the sun to two different spots. As the facets are not mounted in a plane that goes through the central axis of the tube, the weight also produces a torque that twists it. The direct radiation on the front side of the tube causes a spatial temperature gradient that makes it bend backward in the same direction as gravity loads and hence makes the focus to split up even more.

Truss. The trusses are not exposed to sunlight so there is no temperature gradient to be expected, but they bent due to the weight of the facets. Although this does not contribute to the splitting in two parts, it will cause the focus to blur and therefore will be included in the model.

Facets. CIEMAT performed Finite Element Method (FEM) calculations with the help of the computer program ANSYS that show the sufficient stiffness and quality of the facets in their metal frame in all positions /CIEMAT 1994/. Therefore the facets are assumed to be ideally stiff, the distortions of the facets with different elevation angles or temperatures are not considered.

Others. Any inaccuracies or play in the drives, connections and bearings are not considered.

4.4 Mathematical Models for GM-100 Behaviour

In order to describe the behavior of the heliostat mathematically, some basic definitions are needed. The coordinate system used at the PSA has its origin in the center of the concentrator

plane. The facets are in the x-y-plane with the y-axis parallel to the torque tube (east positive), the x-axis in the direction of the trusses (downwards positive) and the z-axis perpendicular to this plane with positive values in the direction of the reflected rays (Fig. 4-4). The elevation angle is called elev and is defined as zero with the facets in vertical position. Higher elevation angles are defined positive. The azimuth angle is zero when facing south, positive when facing east and negative when facing west.

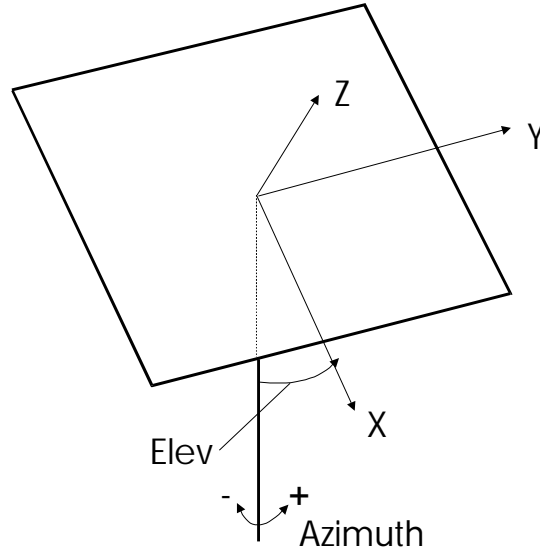


Fig. 4-4: Definitions of the used Coordinate System

Calculations with a very detailed geometry and simulations of the dynamic behavior of the heliostat can only be done with a powerful software tool, such as the FEM-program ANSYS /ANSYS 1997/. This was not available at the PSA, therefore the model must be simplified to its main structural parts and static loads. The rather complex problem of the deformation of the whole support structure can be split in several smaller problems. All the structural parts and load cases (temperature, gravity loads) are regarded separately. This way the deformations can then be calculated more easily and in the end they can be linearly superimposed /KUSSMAUL 1994/.

4.4.1 Gravity Loads of the Pedestal

The simplified geometry of the pedestal can be seen in Fig. 4-5. It consists of a 4000 mm long (L_{ped}) steel tube with an outer diameter D_{ped} of 600 mm and a thickness t_{ped} of 16 mm. It is rigidly mounted on a concrete foundation with screws. On top of the pedestal is the elevation drive that moves the torque tube with the help of a lever of the length e . The weight of the 32 facets ($m_{32facets}$), 8 trusses ($m_{8trusses}$) and torque tube (m_{tube}) induces the force F_{conc} .

$$F_{conc} = (m_{32facets} + m_{8trusses} + m_{tube}) \cdot g \quad (4-4)$$

This force causes the moment:

$$M_{b,ped} = F_{conc} \cdot e \cdot \cos(elev + 60^\circ) \quad (4-5)$$

The additional angle of 60° comes from the mounting geometry (Fig. 4-1). The moment $M_{b,ped}$ changes with the elevation angle and has the same value over the whole length of the pedestal. This causes the tube to tilt forward about the angle /DUBBEL 1986/:

$$\Delta elev = \frac{M_{b,ped} \cdot L_{ped}}{E \cdot I} \quad (4-6)$$

With E : Young's Modulus
 I : Moment of Inertia

The resulting z-displacement of the mirror plane is

$$\Delta z_{ped,g}(x) = -\Delta elev \cdot x \quad (4-7)$$

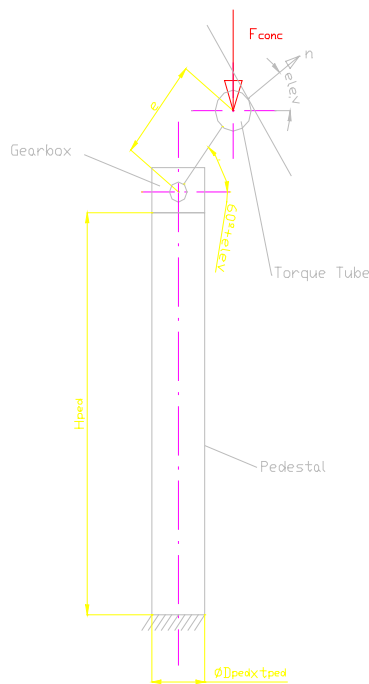


Fig. 4-5: Simplified Model of the Pedestal

4.4.2 Gravity Loads of the Torque Tube

The simplified model of the torque tube is shown in Fig. 4-6. Its geometry and loads are symmetrical, therefore it is sufficient to calculate the deformations for one side only. The figure shows just the right half of the tube. But it is necessary to consider the correct boundary conditions. In the cutting plane the tube can move within the y-z-plane, but not in the x-direction. This corresponds to the bearings shown. Additionally, there is an inner moment $M_{b,tube}$ in the cutting plane that needs to be considered in order to satisfy the equilibrium of forces and moments. The boundary conditions of the tube given mathematically are $z'(0)=0$ and $z(0)=0$ per definition of the coordinate system.

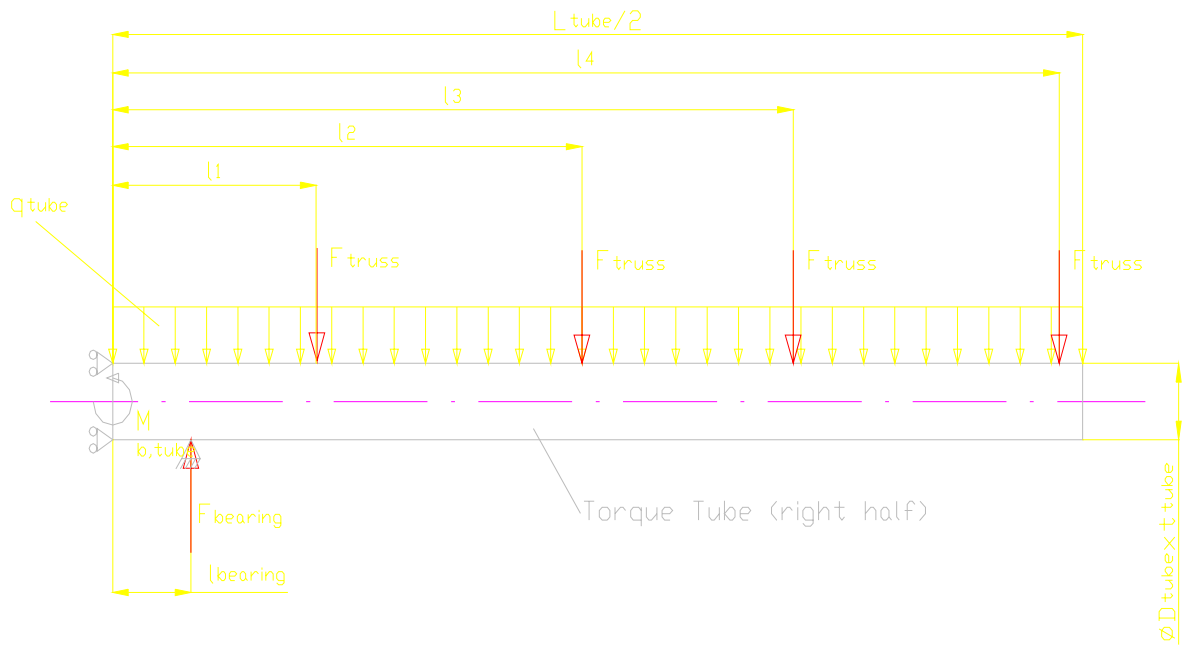


Fig. 4-6: Simplified Model of one Side of the Torque Tube

The steel tube has a thickness of $t_{tube}=16\text{ mm}$, an outer diameter of $D_{tube}=406.4\text{ mm}$ and its half length is $L_{tube}/2=6200\text{ mm}$. The support is in the distance of $l_{bearing}=500\text{ mm}$ and the trusses are mounted in the distances l_1 to l_4 . The weight of the facets and the trusses induce the forces

$$F_{truss} = -(m_{4, facets} + m_{1, truss}) \cdot g \quad (4-8)$$

while the weight of the tube itself is modeled as the area load q_{tube} .

$$q_{tube} = -A_{tube} \cdot \rho_{steel} \cdot g \quad (4-9)$$

From the equilibrium of forces it is known that the reaction force in the bearing is

$$F_{bearing} = -(4 \cdot F_{truss} + q_{tube} \cdot \frac{L_{tube}}{2}) \quad (4-10)$$

From the equilibrium of moments results the inner moment

$$M_{b, tube} = -F_{truss} \cdot (l_1 + l_2 + l_3 + l_4) - F_{bearing} \cdot l_{bearing} - \frac{\left(\frac{L_{tube}}{2}\right)^2 \cdot q_{tube}}{2} \quad (4-11)$$

Bending. With all this information given, the deformations due to bending can be calculated using the formulas of a beam /MAGNUS MÜLLER 1990/. The so called bracket function is needed to formulate the different fields in one equation. It is defined as follows:

$$\{x - \xi\}^p = \begin{cases} (x - \xi)^p & \text{for } x > \xi \\ 0 & \text{for } x < \xi \end{cases} \quad (4-12)$$

With this tool the mathematical relations are the following. The specific length load is:

$$q(x) = q_{tube} \cdot \quad (4-13)$$

Integrating this and adding the point loads, the transverse force is obtained:

$$Q(x) = -F_{bearing} \{x - l_{bearing}\}^0 - F_{truss} \left(\{x - l_1\}^0 + \{x - l_2\}^0 + \{x - l_3\}^0 + \{x - l_4\}^0 \right) - q_{tube} \cdot x \quad (4-14)$$

In order to get the distribution of the inner moment, the equation needs to be integrated again and the moments to be added:

$$M(x) = M_b - F_{bearing} \{x - l_{bearing}\}^1 - F_{truss} \left(\{x - l_1\}^1 + \{x - l_2\}^1 + \{x - l_3\}^1 + \{x - l_4\}^1 \right) - \frac{q_{tube}}{2} x^2 \quad (4-15)$$

The moment is proportional to the second derivation of the bending line. This describes equation 4-16, where E is Young's Modulus and I is the moment of inertia:

$$M(x) = -E \cdot I \cdot w''(x) \quad (4-16)$$

Solving for $w''(x)$ and integrating again leads to the gradient of the bending line:

$$w'(x) = -\frac{1}{E \cdot I} \cdot \left[M_{b,tube} \cdot x - \frac{F_{bearing}}{2} \{x - l_{bearing}\}^2 - \frac{F_{truss}}{2} \left(\{x - l_1\}^2 + \{x - l_2\}^2 + \{x - l_3\}^2 + \{x - l_4\}^2 \right) - \frac{q_{tube}}{6} x^3 \right] \quad (4-17)$$

Finally the fourth integration results in the equation of the bending line of the torque tube:

$$w(x) = -\frac{1}{E \cdot I} \cdot \left[\frac{M_{b,tube}}{2} \cdot x^2 - \frac{F_{bearing}}{6} \{x - l_{bearing}\}^3 - \frac{F_{truss}}{6} \left(\{x - l_1\}^3 + \{x - l_2\}^3 + \{x - l_3\}^3 + \{x - l_4\}^3 \right) - \frac{q_{tube}}{24} x^4 \right] \quad (4-18)$$

The torque tube always has this arched shape due to the gravitational forces. The facets, however, change their position in proportion to this arc. Hence, the displacements in z-direction of the facets are independent of the distance from the tube (y), but depend on the distance in x-direction and on the elevation angle as shown in Fig. 4-7:

$$\Delta z_{tube,bending,g}(x) = \sin(elev) \cdot w(x) \quad (4-19)$$

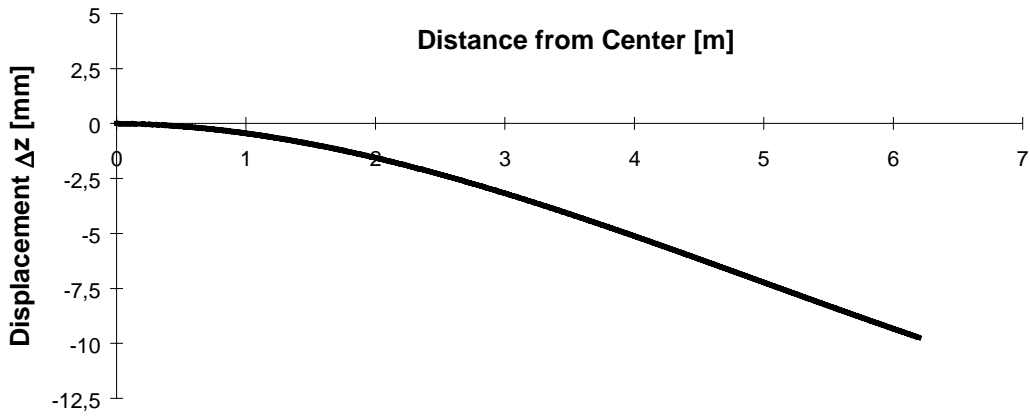


Fig. 4-7: Bending Line of Torque Tube due to Gravity

Torque. The center of gravity of the concentrator is not located in the axis of the tube, but at the distance a from the axis. The facets are mounted close to tangential to the torque tube, hence the distance a is supposed to be the radius of the torque tube. This induces a torque that twists the tube and that is dependent on the elevation angle. Equation 4-20 describes the torque that results from the gravity force and lever of each truss as seen in Fig. 4-6:

$$M_{truss} = m_{4\text{facets}} \cdot g \cdot a \cdot \cos(\text{elev}) \quad (4-20)$$

Then the twisting angle φ of the torque tube in the distance x can be calculated by using equation 4-21 with the respective moments and lengths:

$$\varphi(x) = \frac{M_{truss} \cdot (x - l_{bearing})}{G \cdot I_p} \cdot (4 - \{x - l_1\}^0 - \{x - l_2\}^0 - \{x - l_3\}^0 - \{x - l_4\}^0) \quad (4-21)$$

for $x > l_{bearing}$, with G : Shear Modulus
 I_p : Axial Moment of Inertia

The displacement in z-direction not only depends on the twisting angle, but also on the distance y from the tube:

$$\Delta z_{tube,torque,g}(x, y) = \sin(\varphi(x)) \cdot y \quad (4-22)$$

4.4.3 Gravity Loads of the Trusses

The trusses form plane frames as shown in Fig. 4-8. The weight of the facets and the trusses themselves are added up to a single area load q_{truss} that acts over the whole length.

$$q_{truss} = \frac{m_{truss}}{L_{truss}} \quad (4-23)$$

The structure is fixed to the torque tube that is assumed to be ideally rigid.

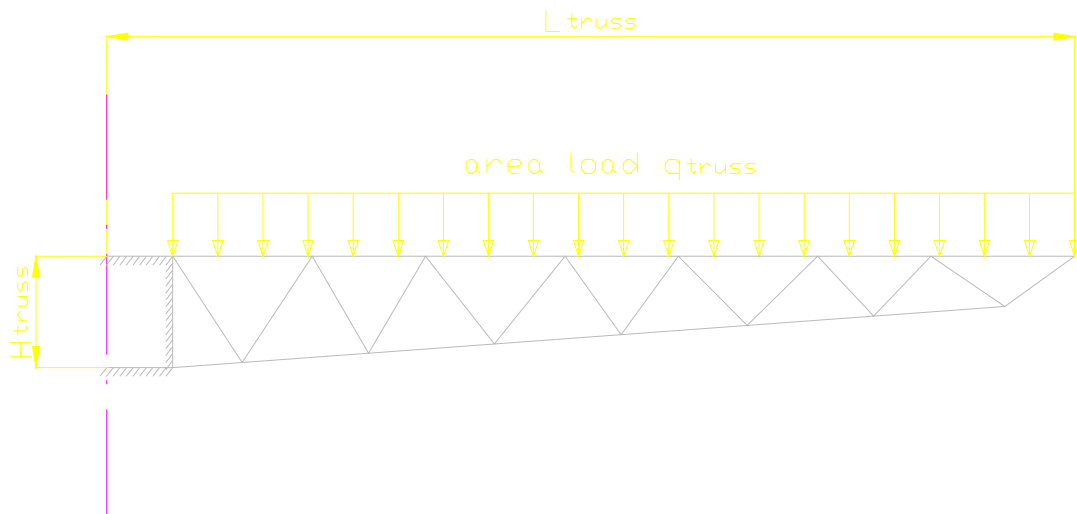


Fig. 4-8: Simplified Model of the Truss

The forces, stresses and deformations of all the bars can be calculated with well-known equations of pin-jointed frames /DUBBEL 1986/. Once the deformations of the bars are known, the deformation of the whole truss can be determined. This was done using a spread-sheet program (Excel 95). The resulting deformation is shown in Fig. 4-9. The points do not form a steady function over x , but they can be approximated very closely by using a third order polynomial trend-line. Considering the elevation angle, the deformation of the truss is obtained:

$$\Delta z_{truss,g} = (0.0095 \cdot |x|^3 - 0.1288 \cdot x^2 - 0.0404 \cdot |x|) \cdot \sin(elev) \quad (4-24)$$

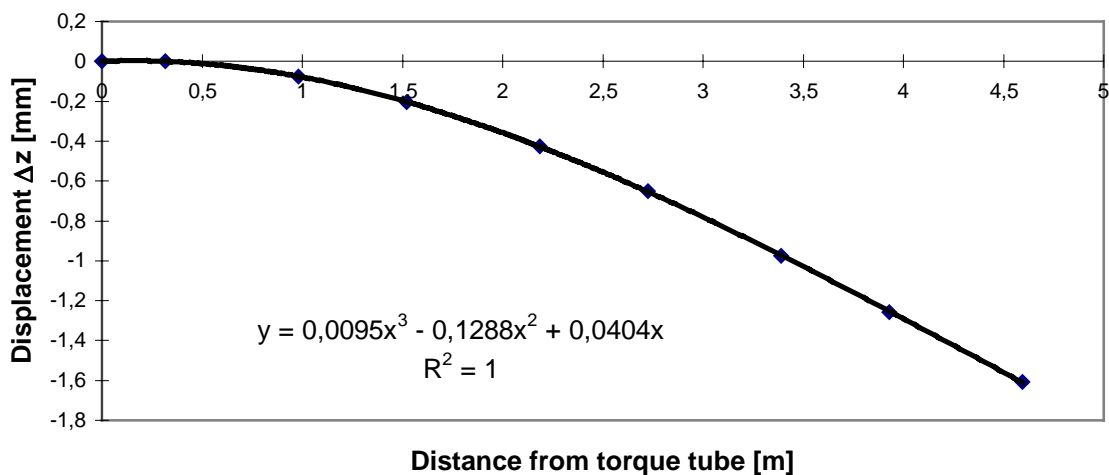


Fig. 4-9: Bending line of truss

4.4.4 Temperature Influence

The changing ambient temperature does not affect the shape of the support structure, whereas the spatial temperature gradient due to solar insolation does. All parts facing the sun will heat up while the parts in the shade stay cooler. The resulting temperature differences make the front side expand more than the backside and hence the structure bends out of shape.

The only parts of the GM-100 support structure that are exposed to direct sunlight are the pedestal and the torque tube. Therefore it is sufficient to find a model for bending of tubes as shown in Fig. 4-10.

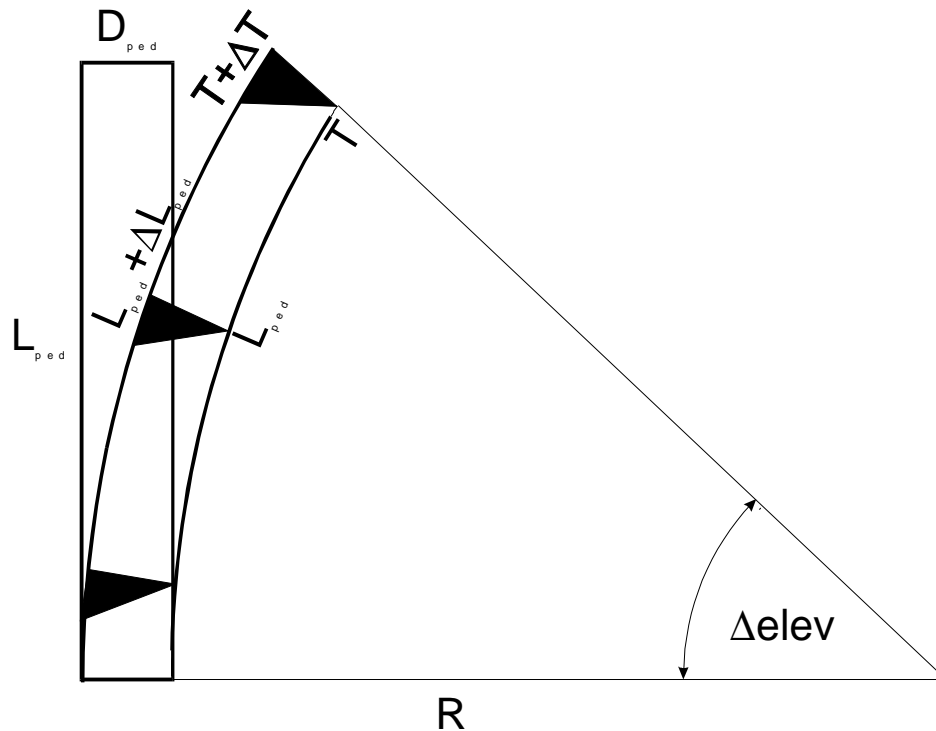


Fig. 4-10: Bending of a Tube due to a Temperature Gradient over the cross-section of the tube

The warmer side expands about the length ΔL_{ped} while the cool side keeps its temperature and length L_{ped} /KUSSMAUL 1994/.

$$\Delta L_{ped} = L_{ped} \cdot \Delta t \cdot \alpha \quad (4-25)$$

with α = temperature coefficient of steel

This causes the tube to bend in an arc with radius R and the resulting tilting angle $\Delta elev$ in radians is:

$$\Delta elev = \frac{L_{ped}}{R} = \frac{\Delta L_{ped}}{D_{ped}} \quad (4-26)$$

The corresponding deformation in z-direction is:

$$\Delta z_{ped,t}(x) = \Delta elev \cdot x \quad (4-27)$$

The bending of the torque tube due to the temperature gradient contributes towards the same direction as the bending due to gravity. Equation 4-28 shows the displacement of the facets in z-direction:

$$\Delta z_{tube,t}(x, \Delta t) = \frac{x \cdot (1 - \Delta t \cdot \alpha)}{D_{torquetube}} \quad (4-28)$$

4.4.5 Wind Loads

Without a powerful software tool based on the finite element method it is not possible to calculate the effects of dynamic wind loads. However, a simple estimation of the deformations caused by a static, frontal wind load can be done. The heliostat is assumed to have the shape of a rectangular plate with the size of 105 m² that is perpendicular to the acting wind ($c_w=1.1$). Then the heliostat receives a drag of /DUBBEL 1986/:

$$F_{w,frontal} = 1.1 \cdot \frac{\rho_{air} \cdot v_{wind}^2}{2} \cdot A_{concentrator} \quad (4-29)$$

This force is supposed to act as an evenly distributed area force. The obtained wind load can be applied to the formulas above to get the displacements in z-direction.

4.4.6 Superimposed Deformations

The deformation of the heliostat as a whole is the sum of all the before derived deformations. As the deformations do not influence each other, the equations can be linearly superimposed as follows:

$$z(x, y, elev, \Delta t_{ped}, \Delta t_{tube}) = \underbrace{\Delta z_{ped,g} + \Delta z_{tube,bending,g} + \Delta z_{tube,torque,g} + \Delta z_{truss,g}}_{gravitation} + \underbrace{\Delta z_{ped,t} + \Delta z_{tube,t}}_{temperature} \quad (4-30)$$

Finally, with all the values put in, the deformation of the concentrator plane from the original shape ($z=0$) is obtained (equation 4-31). In order to simplify the equation, polynoms of up to third order were used as approximations for all the equations except for the analytical solutions for the pedestal. The units of the x- and y-values are meters, the elevation is in radians, the temperature difference in Kelvin and the unit of the z-direction is millimeters.

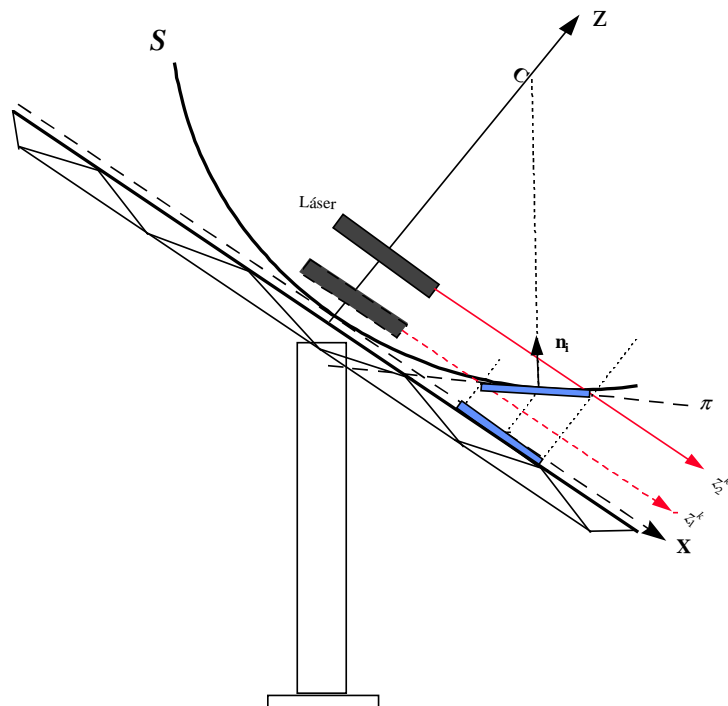
$$\begin{aligned} z(x, y, elev, \Delta t_{ped}, \Delta t_{tube}) = & -0.459 \cdot \cos(elev + 60^\circ) \cdot x \\ & + (0.028 \cdot |y|^3 - 0.4178 \cdot y^2 - 0.0572 \cdot |y|) \cdot \sin(elev) \\ & - 0.0309 \cdot |y| \cdot \cos(elev) \cdot x \\ & + (0.0095 \cdot |x|^3 - 0.1288 \cdot x^2 - 0.0404 \cdot |x|) \cdot \sin(elev) \\ & + 0.08 \cdot \Delta t_{ped} \cdot x \\ & - 0.0148 \cdot \Delta t_{tube} \cdot y^2 \end{aligned} \quad (4-31)$$

5 Measurement Set-Up

It is important to validate the results that are obtained with the mathematical formulas derived earlier. There are several possibilities to do this. One way is to measure the deformations at different elevation angles and temperatures directly at the heliostat with a laser as described below. Another possibility is to compare the calculated focus shape with the real focus shape obtained with the flux measurement system. And yet another proceeding to qualitatively determine the concentrator deformation is by looking backwards from inside the focus towards the reflecting facets. On dusty or slightly foggy days the reflected rays and their orientation can be seen directly and by moving the heliostat slowly in all directions, it can be seen which part of the concentrator is reflecting at the moment and which is not. This gives important information about the actual orientation of the facets. All three methods were used, therefore they are described in detail in the following chapters.

5.1 Set-Up of the Laser Measurements

The deformations of the concentrator plane in z-direction can be measured with the laser set-up usually used for canting (Fig. 5-1).



Canting methodology

Fig. 5-1: Set-up of the new Laser Canting Methodology /MONTERREAL 1997/

The new canting method uses a laser pointer mounted perpendicularly to the z-axis on the torque tube in the center of the heliostat. It can be turned around the z-axis, hence the beam cre-

ates a plane parallel to the x, y-plane. All the points where the laser can be seen are consequently at the same z-elevation. The relative distance of these planes can be measured exactly at the laser set-up in the center. This allows to determine the relative distance in z-direction of every arbitrary point of the concentrator surface. With the z-values of the ideal parabolic shape known from calculations, the facets can be canted at every elevation angle without a target needed.

Using the same set-up, the deformations in z-direction of the support structure can be measured. The expected displacements are rather small, therefore, to verify the calculations, it is best to measure the most deflected parts of the heliostat in the most extreme load cases in order to minimize the relative measurement error. These are the ends of the torque tube and the extreme corners at the elevation angles $\pm 90^\circ$.

The laser will be mounted at 90° elevation and adjusted to produce a plane slightly above and closely parallel to the mirror plane. There is no need to calibrate the system because only relative values and no absolute values are measured. Then the absolute perpendicular distances to the chosen measurement points (Fig. 5-2) are determined in the positions facets up ($elev=90^\circ$), facets down ($elev=-90^\circ$) and early morning ($elev=10^\circ$). This is done by measuring the perpendicular distance from the laser spot to a fixed point with a ruler. By subtracting the absolute distances, the displacements at different elevation angles can be obtained.

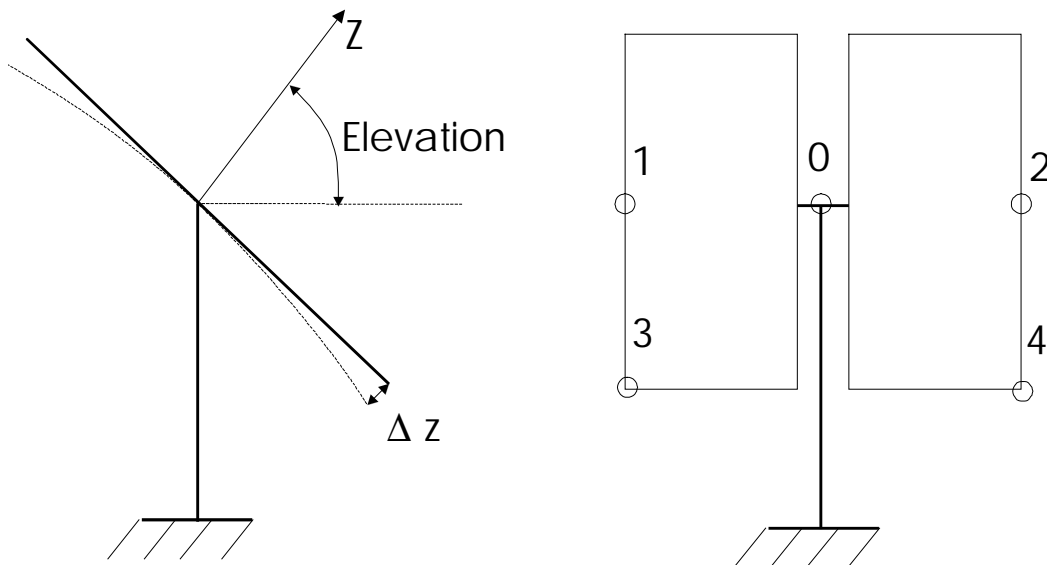


Fig. 5-2: Laser Measurement Points

5.2 Temperature Measurements

It was supposed that the sun heats up the front side of the tubes while the backsides stay cool. In order to verify this statement and to get the actual Δt -values, it is necessary to measure the temperature distribution in the tubes over a whole day. This is done with a special thermometer (Yokogawa, Digital Thermometer Model 2455) that is able to measure the temperature of a surface point with an accuracy of 0.1°C . A styrofoam piece can be used to press the temperature sensor to the surface of the heliostat and so ensure the needed contact. This way the sensor is neither subjected to the direct radiation of the sun nor influenced by the temperature of the

subjected to the direct radiation of the sun nor influenced by the temperature of the experimenter's finger. On a completely sunny day the heliostat is set in tracking mode like in everyday use and then the temperatures of six chosen points are measured every hour. The measuring points are on the front (side facing the sun) and back (side in the shade) of three circumferences: one in the center of the torque tube, one between the facets (1.5 m west of center) and one at the pedestal about 1.5 m above ground as shown in Fig. 5-3.

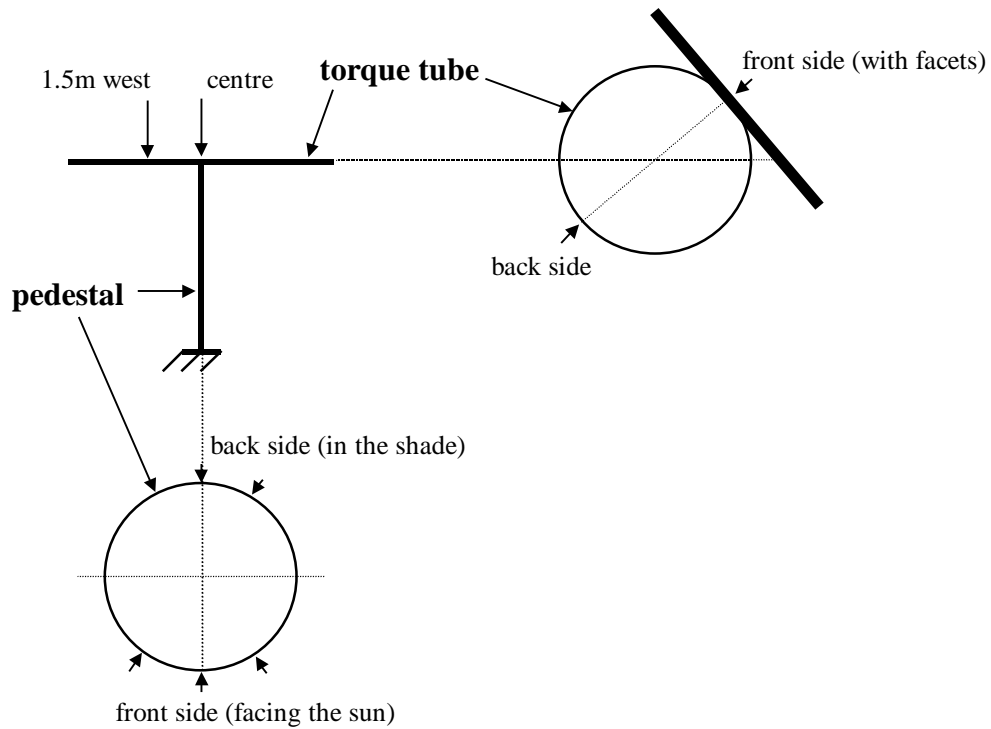


Fig. 5-3: Set-up of Temperature Measurements

With the laser set-up described earlier it is also possible to measure the deformations in the torque tube due to a temperature gradient. This is achieved as follows:

In order to measure the deformations due to temperature influences exclusively and eliminate any deformations due to gravity loads, the heliostat needs to be fixed in a position. The heliostat will be set to an elevation of about 70° and facing south. That way the torque tube receives the highest insolation possible when facing the sun at solar noon and the bending due to temperature differences is maximized. In the morning the laser is mounted and the z-distances at the outer ends of the tube are measured with the laser beam as described earlier. Directly after this the temperature distribution in the torque tube is measured as shown above. At solar noon (approx. 2 p.m. in Almería during summertime) the same measurements are taken again. With the differences in the temperature gradients and Δz values that will be measured it is possible to check the results from the temperature calculations.

5.3 Flux Measurement

The pictures of the flux distribution of the beam were taken with the PROHERMES flux measurement system /HOLLÄNDER 1998/ whose set-up is shown in Fig. 5-4. It is a non-direct measurement system that makes use of an ideal diffuse reflecting surface and a video camera. As

shown, the target is positioned outside the tower under the receiver. The directed solar radiation reflected by the heliostat hits the target surface. There the radiation is diffusely reflected by a Lambertian Target (absolutely diffuse reflecting surfaces are named as Lambertian in thermodynamics /BAEHR 1996/). The reflected radiation is directly proportional to the incident radiation and therefore a measure of the incident radiation flux density.

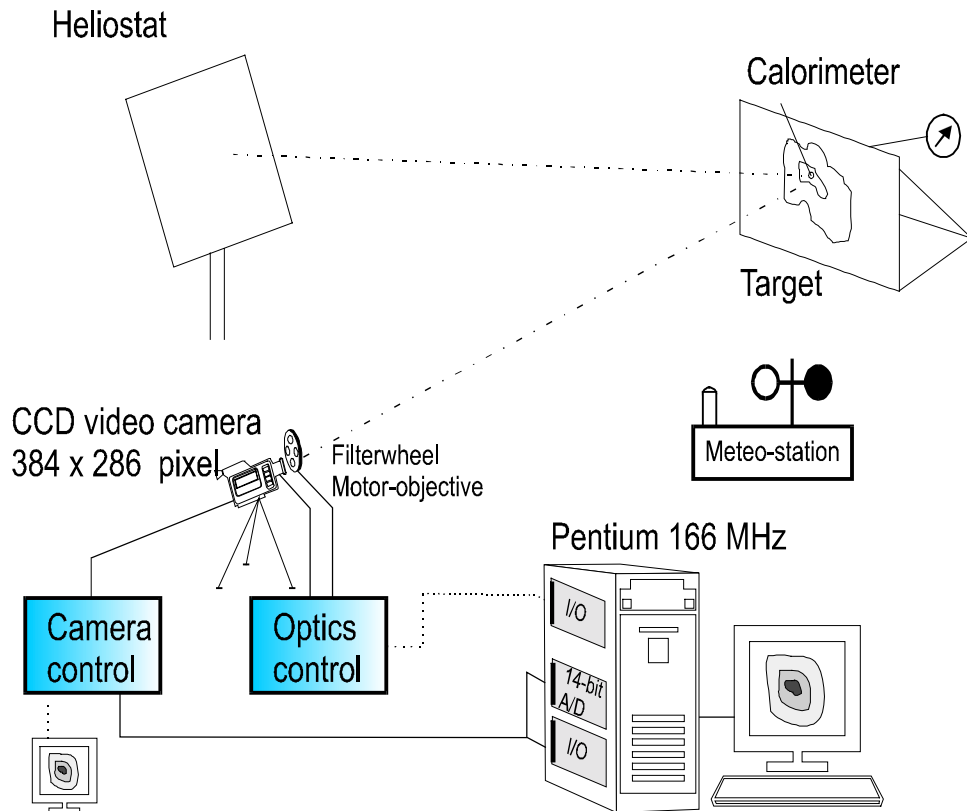


Fig. 5-4: PROHERMES Flux Measurement Set-up

The reflected radiation is recorded by a video camera. The output data of the camera is a matrix of gray scale values that is transferred to a computer, where an analysis is made by OPTIMASTM, a special image processing software /OPTIMAS 1996/.

The video camera only provides relative measuring signals. To obtain absolute values, it is necessary to determine the relationship between these relative scale values and an absolute scale of flux density. Therefore, the intensity on a defined coordinate on the target is compared with the signal achieved by a calorimeter in the same coordinate /FINKENWIRTH 1997/.

6 Results

All results obtained in the above described experiments and calculations are given and discussed in this chapter. To avoid confusion they are split in two parts: the measurements and the calculations. Based on the results, the consequences on possible cost reductions are discussed in paragraph 6.3. Finally, possible design improvements to avoid unwanted consequences are proposed.

6.1 Measurements Results and Assessment

This paragraph shows the results of the measurements described earlier. The directly corresponding calculated values are given as well, so that they can be compared and discussed.

6.1.1 Deformation of the Torque Tube

Table 6-1 shows the results of the deformation measurements of the torque tube on April, 21st, 1998. The absolute values at three different elevation angles (10°, 90°, -90°) are the actually measured distances, the mean value is the calculated mean value of the two extreme elevations -90° and 90°, the Δz -measured is the respective difference between measured value and mean value, and the Δz -calculated is the result of the calculation for the respective point and elevation angle. The meteo data show a sunny and quite windy spring day with regular temperatures and radiation.

The measurements show a maximum deflection of the torque tube at its outer ends of ± 7 mm (at -90°/90°) and a maximum deflection of the corners of $\pm 9.0/\pm 9.5$ mm. This corresponds to a deflection of the trusses of 2.0/2.5 mm. The calculated measurements predict a slightly higher deflection of the torque tube (± 9.7 mm) and a little less deflection of the trusses (± 1.7 mm) which add up to ± 11.4 mm maximum deflection of the corners. The measured values for 10° elevation exhibit some fluctuations but in general correspond to the calculated values.

This confirms that the predicted deformations actually occur and that they are in the range of the calculations. The experimental values may have errors due to the inaccuracy in the measuring of the distance, the movement of the heliostat due to windloads (about 20 km/h) and the deformations due to temperature influences that are not considered (measurements took about 2 hours). This may explain the little differences between measurements and calculations, hence, these values are considered a good validation of the calculations.

Table 6-1: Results of the Deformation Measurements on April, 21st, 1998

	Unit	Absolute value			Mean value	Δz measured			Δz calculated		
		10°	90°	-90°		10°	90°	-90°	10°	90°	-90°
z point 0	[mm]	241	241	241	241	0	0	0	0	0	0
z point 1	[mm]	263	266	252	259	-4	-7	+7	-1.2	-9.7	+9.7
z point 2	[mm]	230	235	221	228	-2	-7	+7	-1.2	-9.7	+9.7
z point 3	[mm]	51	58	39	48.5	-2.5	-9.5	+9.5	-2.5	-11.4	+11.4
z point 4	[mm]	10	19	1	10	0	-9	+9	-2.5	-11.4	+11.4
Time		10:30	11:15	12:15							
Ambient Temperature	[°C]	18.1	19.3	19.7							
Wind Speed	[km/h]	16.5	27.9	24.7							
Direct Radiation	[W/m ²]	800	840	870							

6.1.2 Measured Surface Temperature Development

Table 6-2 shows the results of the temperature measurements on June, 9th, 1998. The temperature at the three circumferences were measured every hour, displayed are the temperatures on the sunny side, the shady side and the temperature difference.

Table 6-2: Results of the Temperature Measurements on June, 9th, 1998

Time	Torque Tube Center			Torque Tube 1.5 m out of Center			Pedestal 1.5 m above Ground		
	Sunny Side	Shady Side	Difference Δt	Sunny Side	Shady Side	Difference Δt	Sunny Side	Shady Side	Difference Δt
9:10	21.7	19.6	2.1	22.3	20.6	1.7	24	21.6	2.4
10:10	25	22.8	2.2	25.1	23.9	1.2	25	23.5	1.5
11:10	29	26.3	2.7	28.5	25.8	2.7	26.8	25.6	1.2
12:10	33.5	28.2	5.3	29.5	27.9	1.6	28.3	27	1.3
13:10	32.4	29.9	2.5	31.4	29.7	1.7	29.6	28.4	1.2
14:10	34	31.4	2.6	31.1	30.8	0.3	33.1	29.8	3.3
15:10	33.5	31.9	1.6	31.3	31.1	0.2	32.7	31.2	1.5
16:10	33.7	32.6	1.1	32	31.7	0.3	32.3	31.5	0.8
17:10	33.8	32.2	1.6	32.5	31.9	0.6	32.6	31.2	1.4
18:10	33	32	1.0	31.9	31.1	0.8	32.1	30.8	1.3

The development of the surface temperatures of the torque tube and the pedestal are visualized in Fig. 6-1. The temperatures on the front and on the back at three different circumferences are shown in three graphs. The distance between the two curves (dark color) in vertical direction at a certain time is proportional to the spatial temperature gradient of interest.

At the beginning of the measurements at 9:00h, the torque tube already has a temperature difference of 2 K. The front temperature rises fast in the morning hours, has a peak at 12:00h and again at 14:00 (solar noon). In the afternoon it stays fairly on the same level. The temperature at back rises first with the same velocity but then slightly slower. It has only one peak around 16:30h. This results in the highest temperature differences in the torque tube in the late morning hours and around solar noon (up to more than 5 K), in the late afternoon they are less (1 K - 1.5 K). The temperature difference in the center of the torque tube is higher than in the outer parts, this can be explained with the partial shading effect of the facets. The general development in the outer part is the same, the biggest differences are in the late morning until solar noon, later there is almost no difference at all.

The temperature difference in the pedestal is at first 2 K (the very low morning sun hits the pedestal while the heliostat is in stow position), then it goes down to about 1 K the whole morning because the pedestal is in the shade of the facets. At solar noon the sun hits the pedestal through the gap between the facets, therefore the front temperature gets a peak. Later in the afternoon the temperatures are again closer together.

The temperature development depends on many factors: the irradiation, the wind (cooling), the ambient temperature etc., therefore it will be different every day and difficult to measure. Nevertheless, the taken measurements give an idea of the temperature range and their development and they will be taken as base for the calculations of the focus development. To simplify the calculations, the temperatures of the torque tube center will be taken for the whole tube (temperature differences at the center have the biggest influence and the relative temperature differences further out are basically the same, just with lower absolute values). Unfortunately, there are no data for the canting day available, therefore a mean value for the time around solar noon will be taken for the calculations: 3 K temperature difference torque tube and 3 K temperature difference for the pedestal.

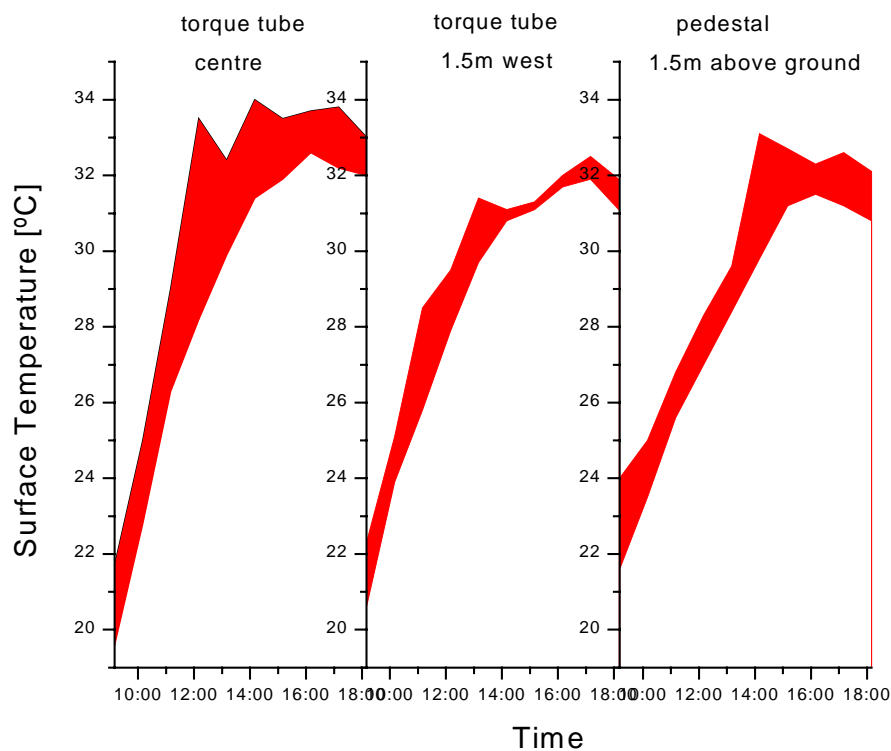


Fig. 6-1: Development of Surface Temperatures on June 9th 1998

6.1.3 Deformation due to Spatial Temperature Gradient

The measurements of the deformations of the torque tube due to temperature only (Table 6-3), in a fixed heliostat position, also show an acceptable agreement with the calculations (calculated

1.0/0.4 mm, measured 1.0 mm). Unfortunately, the values are rather small, therefore it is just a tool to validate the prediction of the range and direction of the deformations. This time, however, the uncertainties of the experimental set-up are reduced to the measurement error only, because there was only little wind and the temperature deflection is considered.

Table 6-3: Results of the Temperature and Deformation Measurements on June, 2nd, 1998

	Unit	11:15 a.m.	2:00 p.m.	Measured Difference	Calculated Deformation
Temp. at front, center of tube	[°C]	24.8	32	7.2	
Temp. at back, center of tube	[°C]	23.4	29.9	6.5	
Temperature difference	[°C]	1.4	2.1	0.7	
Temp. at front, 1.5 m out of center	[°C]	24.9	31.7	6.8	
Temp. at back, 1.5 m out of center	[°C]	24.9	29.9	5.0	
Temperature difference	[°C]	0.0	1.8	1.8	
z value (eastern end of tube)	[mm]	189.5	190.5	1.0	0.4^A/1.0^B
z value (western end of tube)	[mm]	149.0	150.0	1.0	0.4^A/1.0^B
Ambient Temperature	[°C]	27.2	30.5		
Wind speed	[km/h]	4.7	8.1		
Direct radiation	[W/m ²]	784	850		

A: Δt_{center}

B: $\Delta t_{1.5\text{m}}$

6.1.4 Daily Focus Development

Fig. 6-2 shows the daily focus development of the GM-100 on the target. These pictures were taken hourly with the PROHERMES measuring system on two different days. The morning pictures were taken on June, 6th, 1998 until the focus started to leave the target due to tracking problems. With the focus re-centered in the afternoon, the missing pictures were taken on July, 6th, 1998. The target has a size of 12 m * 12 m and the values in parentheses are the time differences to solar noon.

Early in the morning, the focus clearly exhibits the earlier described splitting in two spots and also a tilting of the main axis. The spots are comparatively fuzzy. Closer to solar noon, the tilting of the main axis follows the sun, the two spots move closer together and the diameters of the focus spots become smaller. Around solar noon the heliostat has its best optical quality. There is only one, round and well concentrated focus. In the afternoon, the focus starts to move to the upper right corner and leaves the target, therefore the experiment is continued on another day after re-centering. In the afternoon, the focus shows basically the same behavior as in the morning. It tilts with the moving sun, splits up even more and the spots become more and more fuzzy towards sunset.

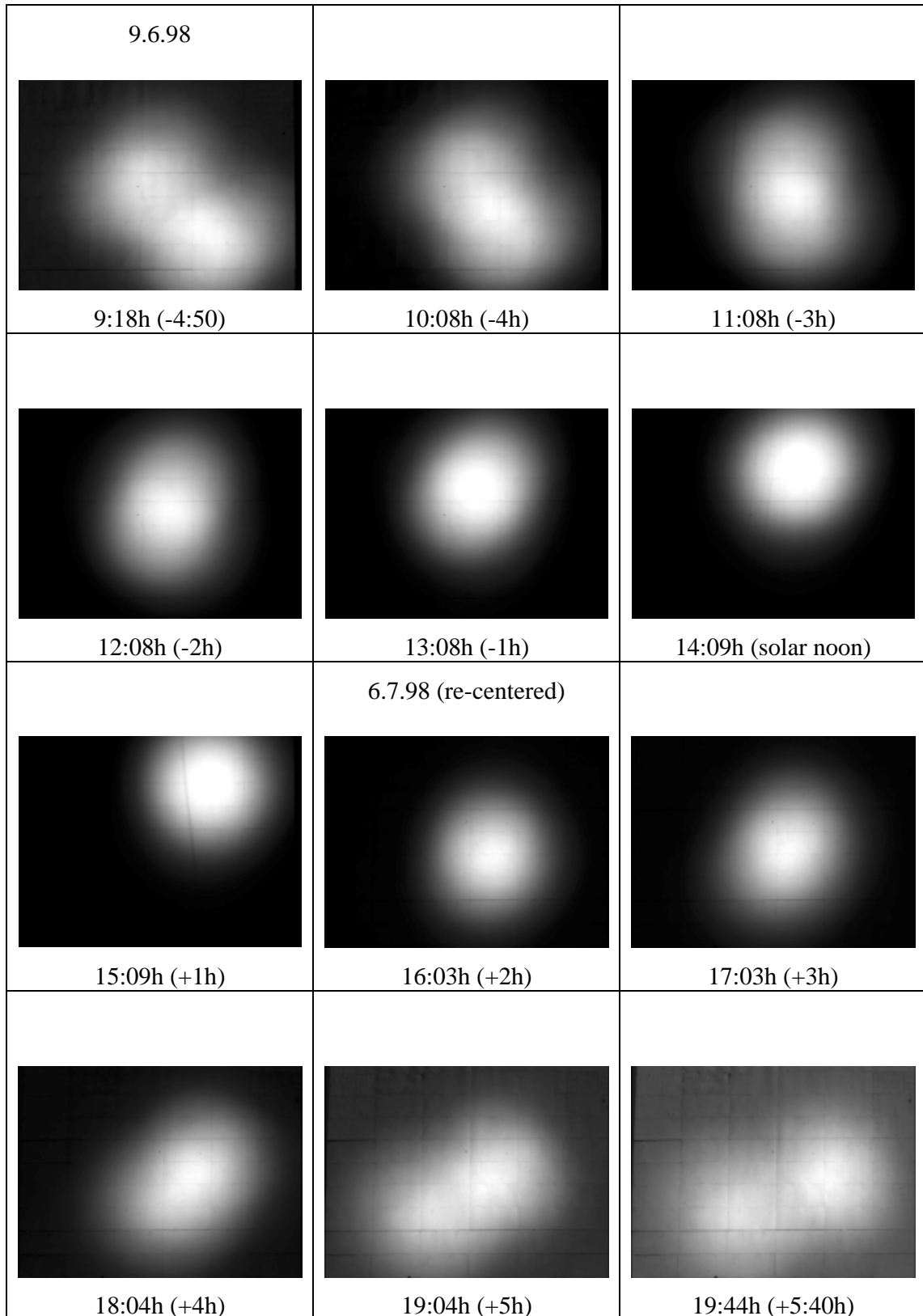


Fig. 6-2: GM-100 Daily Focus Development (time in brackets relative to solar noon)

6.1.5 Pictures of Reflected Rays

Fig. 6-3 shows very illustratively the way of the reflected rays due to the slightly foggy conditions. The picture was taken early in the morning from inside the tower in the opposite direction of the rays. It can be clearly seen that the rays of the eastern and western branch of the GM-100 are two separate beams that cross each other before they meet the target, i.e., the focal distance of the heliostat is less than the slant range.



Fig. 6-3: Reflected rays of the GM-100 early in the morning

6.2 Results of Calculations

This paragraph graphically shows the calculated deformations of the support structure and their consequences for the daily focus development.

6.2.1 Deformation of Support Structure

The formula of deformations of the GM-100 (Equation 4-31) was used in ORIGIN /ORIGIN 1997/ to display the distorted shape at different elevation angles and spatial temperature gradients (Fig. 6-4 - Fig. 6-7). The transparent grid ($z = 0$) corresponds to the ideally rigid plane (mirror face-up) without deformations and the curved colored surface shows the actual shape. On the bottom, the colors are projected in 2-D. The torque tube is situated along the y-axis from -6.2 to 6.2 m and the trusses are in the direction of the x-axis from -4.62 to 4.62 m (south/down to the right). The deformations in z-direction are displayed in millimeters and in different color levels. The deformations are strongly exaggerated (about 200 times).

40° Elevation, $\Delta t_{\text{tube}} = 3.0\text{K}$, $\Delta t_{\text{ped}} = 3.0\text{K}$

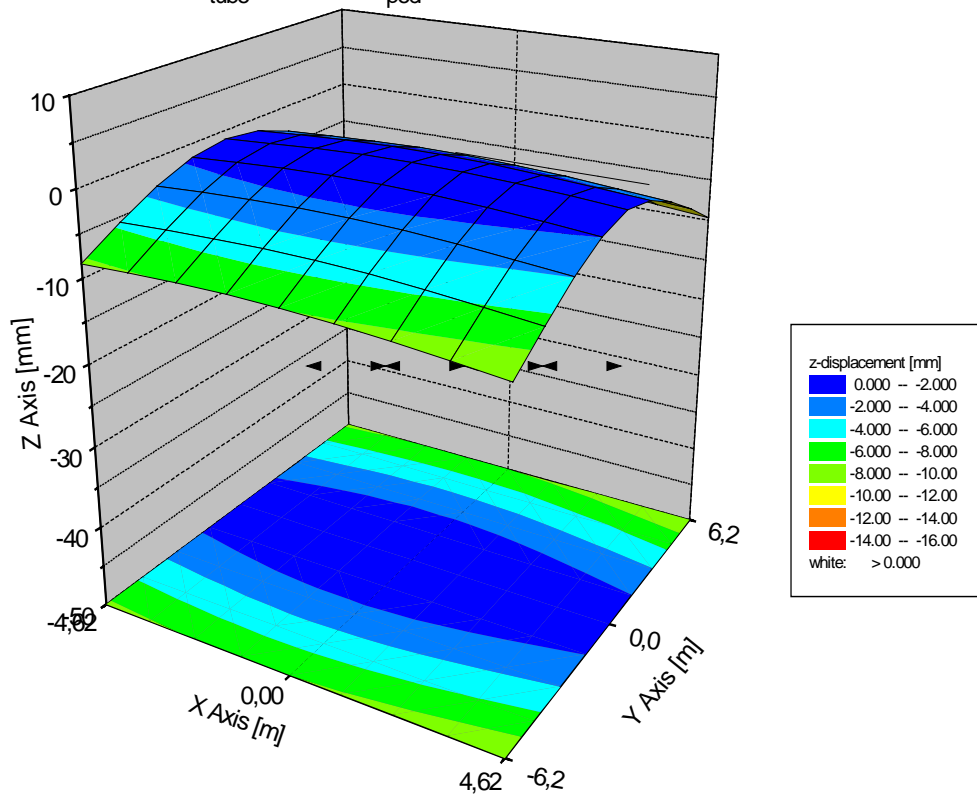


Fig. 6-4: GM-100 deformation at 40° elevation, 3 K temperature difference in torque tube and in pedestal

Fig. 6-4 shows the relative deformations of the GM-100 at an elevation of 40° and a spatial temperature gradient of 3 K in both the pedestal and the torque tube. This load case corresponds closely to the canting point (point in time when the facets are adjusted to the ideal form on July, 18th at solar noon). That means that the heliostat was adjusted to his ideal parabolic shape at the canting point with the support structure already deformed. Therefore all other deformations must be seen relative to the deformations of this load case. The chosen temperature values are averages of the maximum values measured on June, 9th.

It can be clearly seen that the torque tube is responsible for the highest deformations (y-axis), i.e. the east and west branch of the heliostat point in different directions away from each other (the heliostat "opens up"). This is caused by bending due to the weight and additionally by the bending due to the spatial temperature differences that add both up in the same direction. The trusses (x-axis) also show some deformations, these are much smaller though. The tilting of the plane to the back is caused by the bending of the pedestal, mainly due to the temperature difference and very little due to gravitational influence. The torsion of the torque tube has only minor consequences.

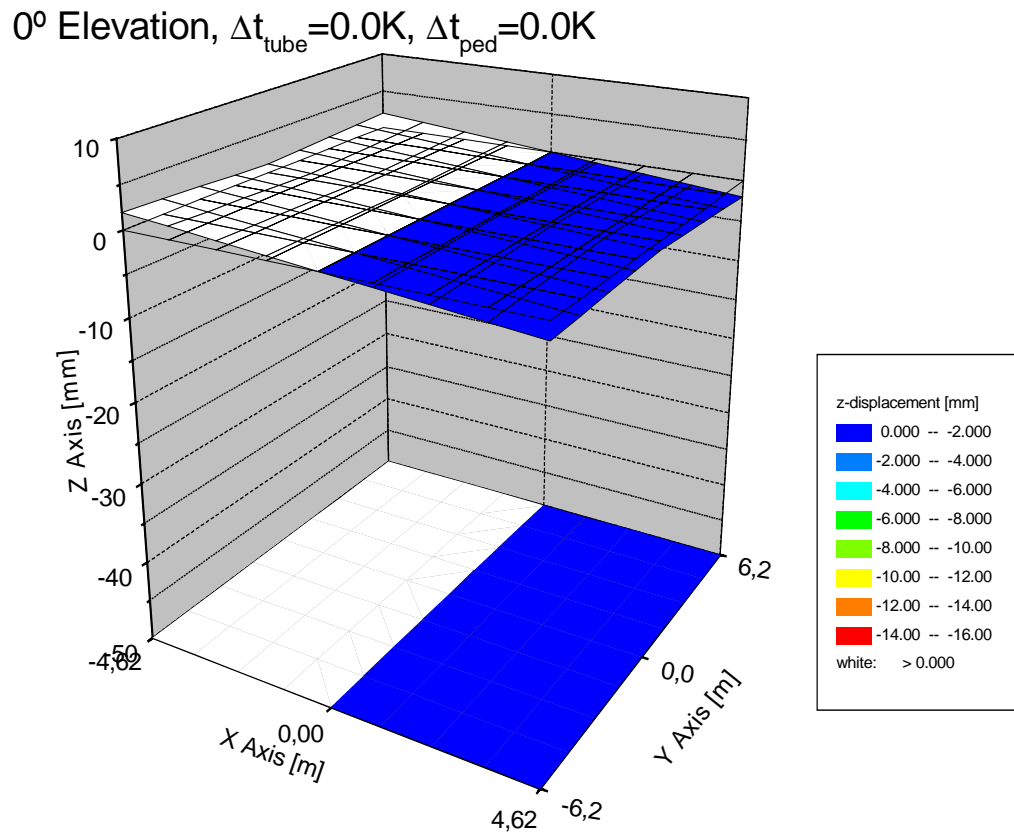


Fig. 6-5: GM-100 deformation at 0° elevation, 0 K temperature difference

Fig. 6-5 shows the deformations in the vertical concentrator position without temperature influences. This load case is close to the early morning conditions when the heliostat has an equal temperature distribution from the night and a very low elevation angle.

It can be seen that the plane is slightly tilted to the front and slightly twisted but the deformations are small. The tilting is caused by the bending of the pedestal and the twisting by the torsion of the torque tube. No other deformations occur.

Relative to the deformations at the canting point this implies a bending of the torque tube to the front, i.e. the surface normals of the two heliostat branches tilt together (the heliostat "closes up"). Therefore, the focal length of the heliostat becomes shorter and the reflected rays cross each other before they hit the target (see picture of crossing rays in Fig. 6-3).

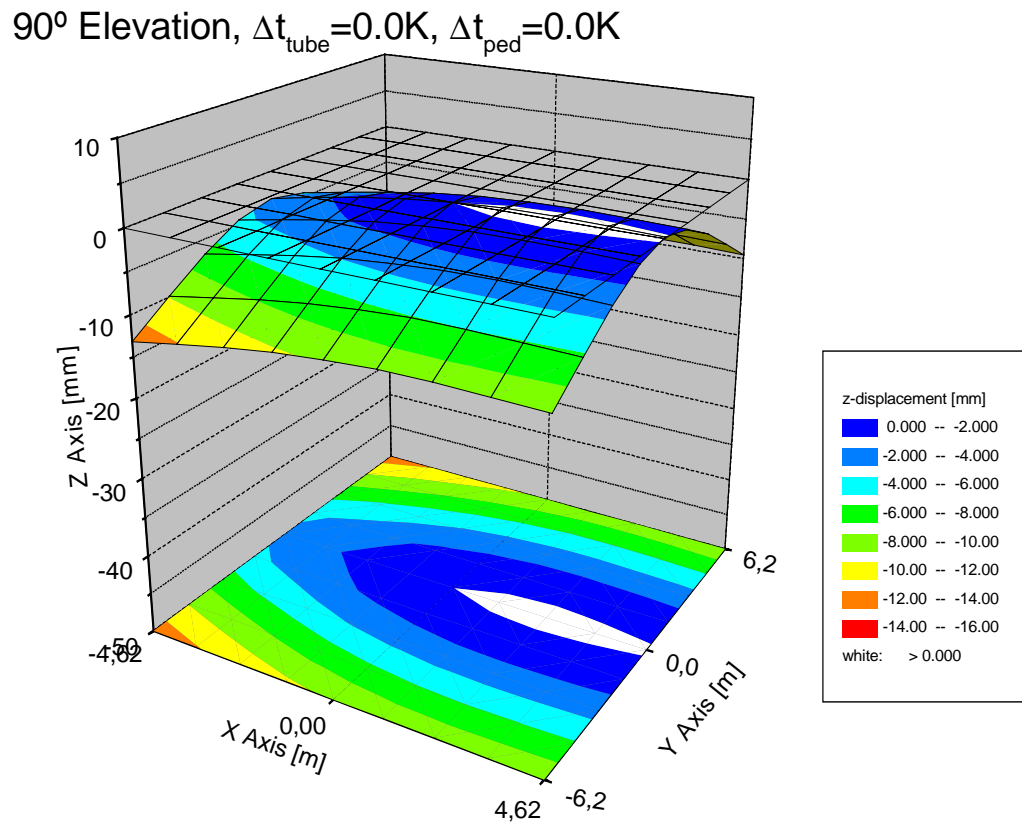


Fig. 6-6: GM-100 deformation at 90° elevation, 0 K temperature difference

Fig. 6-6 shows the deformations with the facets facing up. Although this position is never reached in normal operation, this is the worst load case for deformations due to gravity and is therefore best to observe the structural deformations.

Just as before, the torque tube is responsible for the strongest deformations whereas the trusses show relatively little deformations. The torsion and the tilting cause the upper corners to bend slightly more than the lower corners but generally have only little influences.

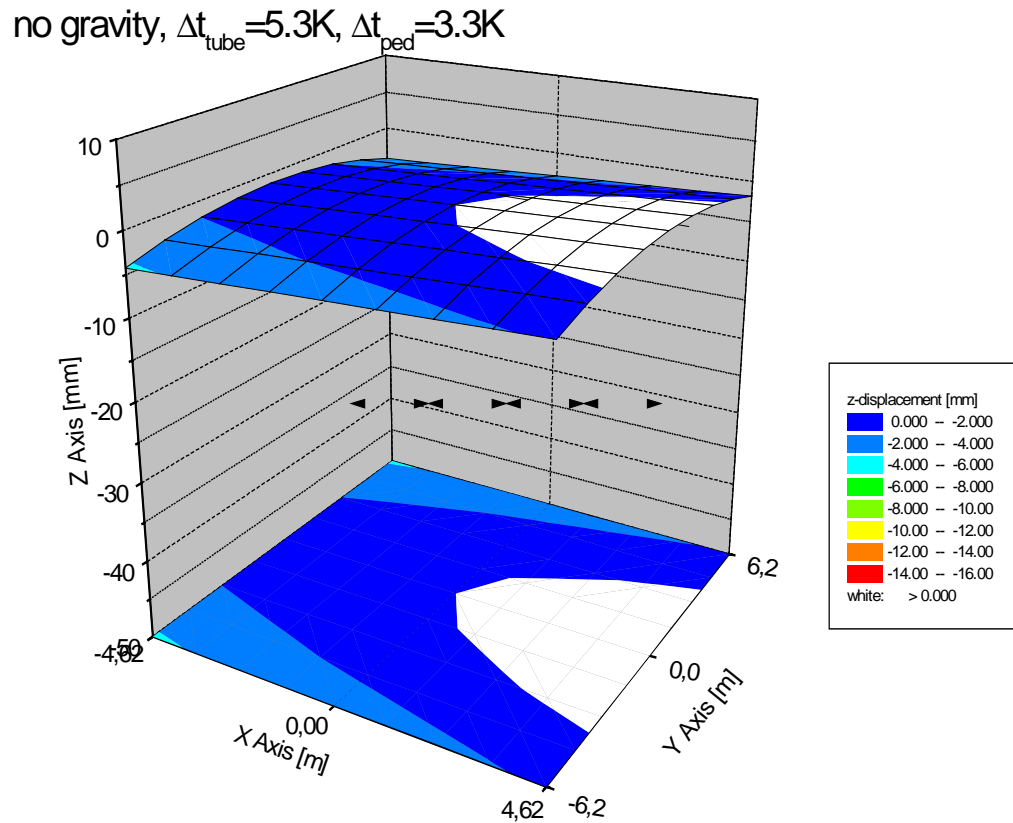


Fig. 6-7: GM-100 deformation with 5.3 K temperature difference in the torque tube and 3.3 K in the pedestal without gravitational influences

Fig. 6-7 shows the consequences of the spatial temperature gradients in the pedestal and the torque tube without gravitational influences. Temperature differences of 5.3 K for the torque tube and 3.3 K for the pedestal were taken. These values correspond to the maximum values measured on June, 9th, 1998.

The overall shape looks very similar to the above, i.e. the deformations due to temperature add up in the same directions to the deformations due to gravity. The pedestal bends backwards in the time around noon and the torque tube bends backward as well.

Table 6-4 gives an overview of the results of the calculations of the deformations at the upper corners ($x = -4.615$ m, $y = \pm 6.2$ m), the outer ends of the torque tube ($x = 0$ m, $y = \pm 6.2$ m), the lower corners ($x = +4.615$ m, $y = \pm 6.2$ m) and the tilting angle of the pedestal. The resulting slope errors and tracking errors are shown in mrad (twice the resulting deviation angle of the surface normal at the outer corners). The results of the laser measurements are displayed in parentheses. The load cases vary in elevation angle (measured in degrees), temperature differences in pedestal and torque tube (K) and wind load (40 km/h is the design point for normal operation).

Table 6-4: Selected Results of Deformation Calculations and Measurements

Load Case	Deformation in z-direction [mm] (without tilting of pedestal)			Tilting angle pedestal [mrad]	Slope Error [mrad]	Tracking Error [mrad]
	x=-4.615m	x=0m	x=+4.615m			
	y= ±6.2m	y= ±6.2m	y= ±6.2m			
0°, 0K	0.77	0.00	-0.77	-0.23	0.27	0.46
90°, 0K	11.38	9.77 (-7.0)*	-11.38 (-9.5)*	0.40	3.97	0.80
-90°, 0K	11.39	9.77 (+7.0)*	11.38 (+9.5)*	-0.40	3.97	0.80
40°, 3K, 3K	-8.33	-7.96	-9.68	0.32	3.37	0.64
no gravity, 5.3K, 3.3K	-3.01	-3.01	-3.01	0.26	1.05	0.53
no gravity, 0K, Wind 40 km/h	-2.11	-1.59	-2.11	0.52	0.55	1.05

*values in parentheses are measured values

The deformations just due to a temperature gradient of 3.3 K in the pedestal and 5.3 K in the torque tube are not very high (1.05 mrad slope error, 0.53 mrad tracking error), but they add up unfavorably in the same direction like the deformations due to gravity loads. Together they make the heliostat "open up" about close to 10 mm in the corners at the canting point (40° elevation, 3.0 K temperature gradient). This corresponds to the relatively large slope error of 3.37 mrad and an acceptable tracking error of 0.64 mrad.

The results of the calculations for a static, frontal wind velocity of 40 km/h without other loads (last line in Table 6-4) show that the structure is relatively insensible to these forces in the concentrator plane (0.55 mrad slope error), the main effect is the bending of the pedestal which results in a tracking error of slightly more than 1 mrad. The deformation due to a static wind load is surely much less than the deformations that can occur due to dynamic wind gusts, it agrees however qualitatively with the observations that can be made on windy days. It can be seen that the focus spot on the target does not change its shape or size dramatically (slope error) but moves in an oscillating motion (tracking error).

6.2.2 Daily Focus Development

With the deformations obtained earlier it is possible to calculate the focus development on the target. A MATLAB program code especially developed for this task was used /MONTERREAL 1998/. The program starts with the rays from the solar disk to the facets, calculates the reflection and the resulting aim point on the target. It considers the elevation and azimuth angle of the heliostat, resulting deflections of the concentrator shape in relation to the canting point, resulting optical effects and errors, heliostat focal length, waviness of the facets (optional), solar disk (optional), and can vary the accuracy and necessary computer power with the grid size of the model.

Fig. 6-8 shows the calculated daily focus development of the GM-100 at the same dates and times like the measurements (Fig. 6-2). The respective elevation and azimuth angles of the sun (calculated) and the temperature difference of the torque tube (measurements, see Table 6-2) used are shown in Table 6-5. The temperature difference of the tubes at the canting point is not known, therefore an estimated mean value of 3.0 K for pedestal and torque tube was used. An

ideal solar disk with an insolation of $1\,000\text{ W/m}^2$ was the input for the sunshape, the facets were supposed to be ideal, i.e. no waviness was considered. In order to keep the computational effort low, each facet was only meshed with a 2x2 grid, therefore the results look somewhat idealized and irregular.

Table 6-5: Input Data for Calculation of Focus Development (Estimated ΔT at canting time: 3.0 K)

Time	Sun Azimuth	Sun Elevation	Δt Torque Tube	Δt to Canting Point
9:18 h	99.1°	27.0°	2.1 K	-0.9 K
10:08 h	92.2°	36.9°	2.2 K	-0.8 K
11:08 h	82.6°	48.8°	2.7 K	-0.3 K
12:08 h	69.4°	60.4°	5.3 K	+2.3 K
13:08 h	46.3°	70.7°	2.5 K	-0.5 K
14:09 h	-0.7°	75.6°	2.6 K	-0.4 K
15:09 h	-46.6°	70.6°	1.6 K	-1.4 K
16:03 h	-66.7°	62.5°	1.1 K	-1.9 K
17:03 h	-80.9°	51.0°	1.6 K	-1.4 K
18:04 h	-91.0°	38.9°	1.0 K	-2.0 K
19:04 h	-99.4°	27.0°	0.7 K	-2.3 K
19:44 h	-104.7°	19.2°	0.5 K	-2.5 K

The results show a very good correspondence with the actual focus deformations (compare Fig. 6-2). Early in the morning the focus is split up in two parts and tilted. Closer to solar noon, the tilting of the main axis follows the sun, the two spots move closer together and the diameter of the focus spot becomes smaller. Around solar noon the heliostat has its best optical quality, there is only one round and well concentrated focus. In the afternoon, the focus shows basically the same behavior as in the morning. It splits up again and tilts its main axis just as seen earlier in the flux measurement pictures. The focus, especially in early morning and late afternoon, is not as fuzzy, this is because of the idealization of the facets and the sunshape. In the visualization of the calculations, the focus was automatically centered, therefore the moving of the center point (tracking error) can not be seen, the pictures are only for comparing the focus shape and size. The calculation predicts a little bit less focus splitting than actually measured, this implies that the temperature difference at the canting point was probably higher than the estimated 3 Kelvin, since a higher spatial temperature gradient during the canting procedure causes a larger focus splitting.

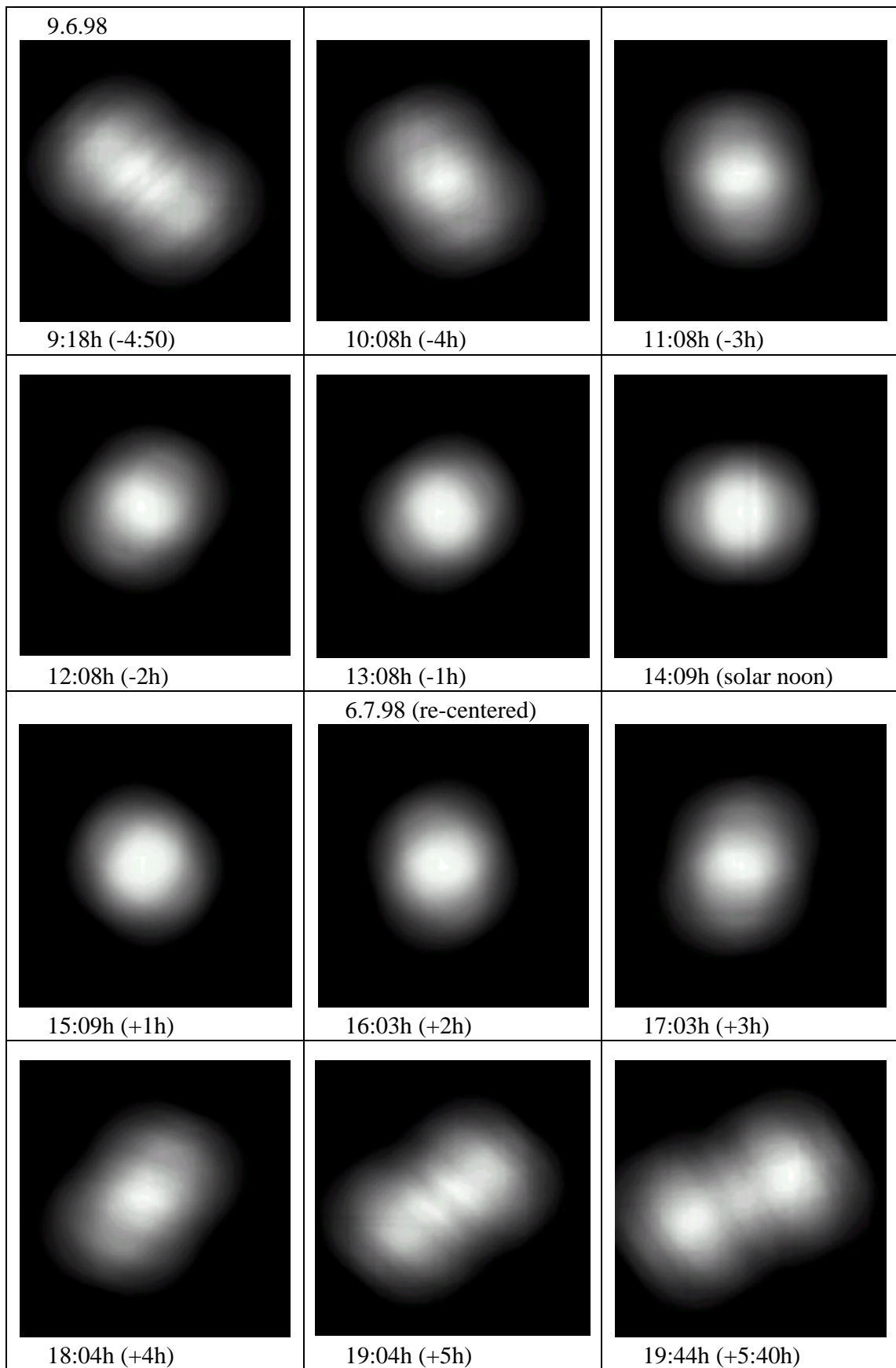


Fig. 6-8: Calculated Daily Focus Development of the GM-100 (time in brackets relative to solar noon)

6.3 Influences of Cost Reduction Measures on Beam Quality

Specific costs of heliostats can be effectively reduced by going to a larger unit size /WILLIAMS 1987/. This allows to distribute the cost for single expensive parts like drive unit, gear box, controller etc. to a larger reflective area and so lower the cost per square meter. On the other hand, bigger constructions of the same type usually increase the structural deformations and hence reduce the beam quality. This is due to the fact that the weight increases with a cubic function whereas the stiffness parameters like cross sectional areas and moments of inertia only increase with a quadratic function. This effect is shown in Fig. 6-9 where the loss of beam quality of a GM-100 type heliostat due to gravitational influences is shown versus the heliostat size. This graph was obtained by varying the magnitude of the GM-100 proportionally. The dotted line shows the beam quality obtained from the mathematical model of this construction for the size of conventional heliostats (40 m^2). Although this is already the new design with a less bulky structure, it shows that for smaller sizes the error due to the bending of the support structure is about in the range of facet errors (1.5 mrad). For larger sizes, the error soon reaches the maximum design value (2.6 mrad), although this does not yet consider temperature or wind influences. The GM-100 at its actual size has a loss of beam quality of more than 2 mrad due to structural deformations.

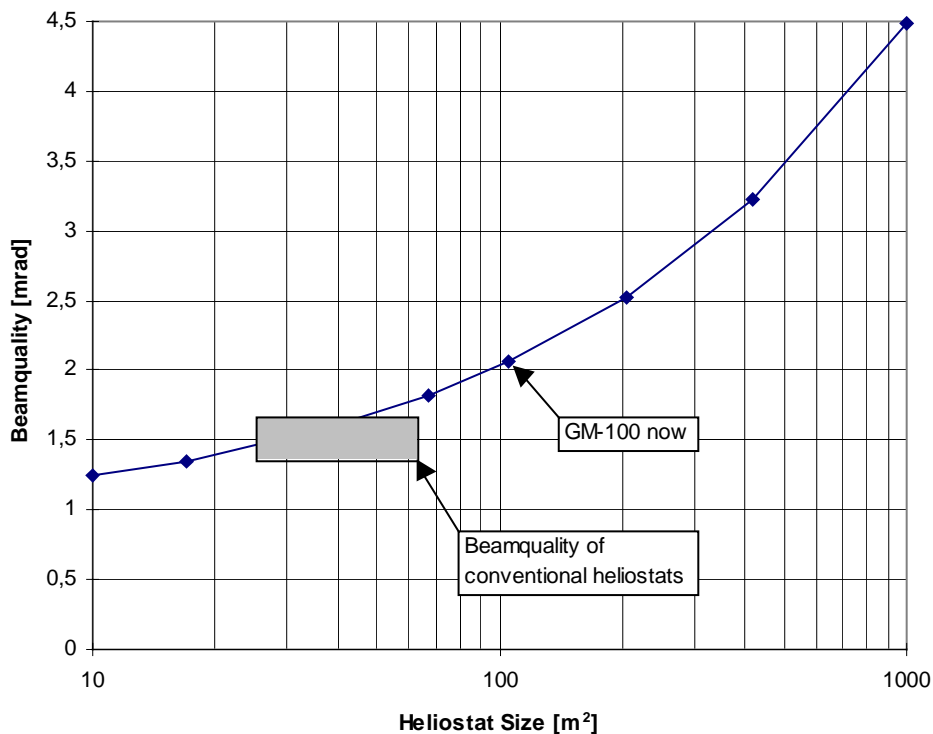


Fig. 6-9: Beam Quality due to Structural Deformations versus Heliostat Size

A larger focus spot results in the loss of energy of the reflected rays that do not hit the receiver aperture (spillage). To avoid energy losses, the receiver aperture can be augmented, but this represents a significant cost factor and again leads to energy losses due to increased radiative and convective losses from the receiver surface. Therefore the aim is to reduce the costs of heliostats

without decreasing the beam quality. This can not be achieved by just increasing their size (see Fig. 6-9) but requires changes in the design of heliostats. Some possibilities of such alterations based on the GM-100 concept are given in the following chapter.

A completely new concept of heliostats, the so-called stretched membrane design, was developed in the last years (e.g. the ASM-150, tested at the PSA). With this concept, the beam quality at large sizes is better and almost independent of gravitational loads. Still, it displays other problems, especially a high wind sensibility of the membrane. In this report, however, the considerations of heliostat improvements will be confined to the T-shaped concept.

6.4 Improvements of Construction

In this paragraph some simple and above all inexpensive improvements of the heliostat will be suggested. Looking at the results of the calculations and measurements, it is obvious that the main fault of the GM-100 is the extensive bending of the torque tube. First of all due to gravitational loading, but also due to the spatial temperature gradient. Therefore, the presented improvements aim mainly on the reduction of bending due to these two effects.

6.4.1 Protection from direct Insolation

The temperature influence can be effectively reduced by protecting the tube from direct sunlight. The facets should be mounted without a significant gap, directly next to each other, to cover the whole tube. In the center an additional sun shield would be necessary, but a simple plastic or tin cover that protects the tube from direct insolation and allows the air to flow in between would do the job. This would efficiently reduce or even exclude the consequences of the hardly to predict spatial temperature gradient.

The new Colon Solar heliostat already shows this improvement /PSA 1997/. The facets are all mounted directly next to each other, forming a continuous plane that completely shades the torque tube and the pedestal. However, this heliostat cannot be stowed face-down.

6.4.2 Modification of the Torque Tube

The stresses in the torque tube in the center are high, whereas the stresses decrease towards the outer ends. Nevertheless, the tube has the same thickness over its whole length. A steadily adapting cross sectional area would be best, but too expensive. To keep it simple, the unnecessary and unfavorable weight of the outer half could be added in the middle and hence improve the stiffness without increasing the material consumption. This could be achieved either by welding two thinner tubes to a thicker one, or by slipping a short, second tube over a thin, long one. This modification cannot be made at the existing prototype at reasonable costs.

6.4.3 Stay Pole

Increasing the stiffness by adding a stay pole in the center towards the front side and cables to the outer ends of the torque tube is still possible. Augmenting the support structure out of the concentrator plane has the positive effect of reducing the bending forces in the torque tube by bear-

ing the weight with normal forces in the cables. This does greatly decrease the stresses and hence the deformations. The thickness of the torque tube and consequently the material consumption could be considerably reduced because it would not have to carry all the loading.

The disadvantages of the pole and the wire construction are a shading of the concentrator surface and a possible handicap for the cleaning of the reflective surface. The shading is rather insignificant, especially during the midday hours when the shadow of the pole becomes very short. The cleaning handicap depends on the used technique, but for high pressure cleaning as applied in trough plants it would not represent a problem.

6.4.4 Composite Materials

The glass/metal facets are very heavy due to the mirror thickness of approximately 4 mm and the required rigid steel frame construction and this is the main reason for the large structural deformations due to gravity. This weight could be effectively reduced with composite materials and a honeycomb structure as it is already widely used in sports equipment like surfboards or other applications where high stiffness and low weight is needed. This lightweight material as a pre-shaped facet backside combined with a thin reflective layer as used in the stretched membrane technology would cut back the high material requirement, the weight and hence the deformations.

6.4.5 Estimated Effects

Fig. 6-10 shows the estimated effects on the beam quality versus the torque tube thickness (4 mm - 16 mm). These calculations were done in R-Stab, a simple 2-D framework program /R-STAB 1996/ that was available in the last month of this study. The deterioration of beam quality due to structural deformations was calculated based on the deformation of the torque tube between an elevation of 0° and 37° (early morning to solar noon) and on the standard deviation formulas shown in chapter 3.2.2.

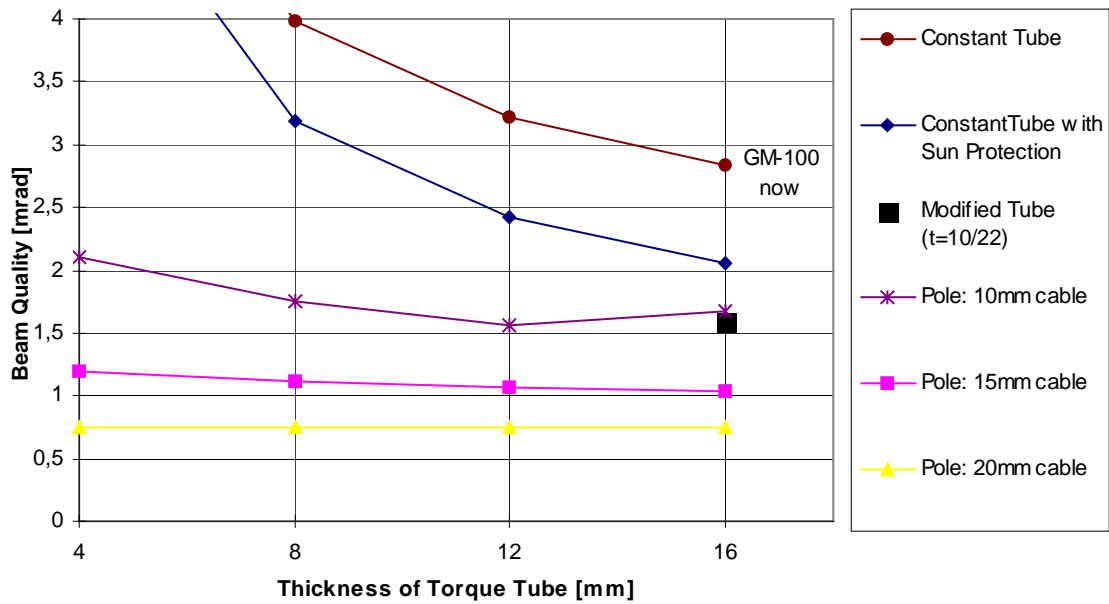


Fig. 6-10: Effects of Design Improvements

The chart shows the performance of the GM-100 heliostat as it is now. The filled circles show the consequences of the reduction of the torque tube thickness without other measures. The curve below (diamonds) displays the improvement due to the elimination of temperature effects (max. 4 K difference, estimated from measurements) with the sun protection. The filled rectangle shows the estimated improvement of the beam quality for a tube with 22 mm thickness in the middle half and 10 mm thickness in its outer halves. Without additional material, the errors due to gravitational loads are reduced by about 25 %. The three curves below display the estimated improvements of the beam quality with the stay pole construction (length $L=3$ m, diameter $\varnothing=100$ mm, thickness $t=10$ mm) and various cables of different diameters (10 mm, 15 mm, 20 mm) versus the tube thickness. The deformations are greatly reduced, even for much thinner torque tubes. In fact, for thick cables the deformations are almost independent of the thickness of the torque tube. That means the construction needs less material, is therefore cheaper and the beam quality is nevertheless much better.

Table 6-6 gives a comparison of the material requirements of the GM-100 and the ASM-150. It can be seen that with 4 320 kg of steel the main contributor to the material requirement of the glass-metal heliostat is the support structure. Using the stay pole construction with an additional weight of less than 100 kg, the torque tube could be reduced from 16 mm walls to 4 mm walls and hence reduce the weight of the tube about 1 440 kg. Further, the calculations of the tilting of the pedestal in Table 6-4 show that the deformations of the pedestal are relatively small and hence the pedestal seems to be oversized. This assumption is also supported by the thinner torque tubes (3÷10 mm) of other large heliostats /GOLDBERG 1991/ /MARTIN MARIETTA 1982/ /MAVIS 1989/. In order to surely avoid error resulting from a too weak foundation, the GM-100 foundation is also by far oversized. A pylon foundation as planned for the AB-66 heliostat and for the first commercial stretched-membrane heliostat would greatly reduce the required concrete and steel for the foundation /ERBE 1997//BROWN 1991/.

With these material reduction measurements it is possible to reduce the specific steel requirements of the GM-100 heliostat to about the those of the ASM-150 heliostat or even less, without the need for a cost and energy expensive high-alloy steel membrane.

Table 6-6: Comparison of the Material Requirements of Large-Area Heliostats /ERBE 1997/

	GM-100				ASM-150			
	Steel	High-alloy	Glass	Concrete	Steel	High-alloy	Glass	Concrete
Drive Unit	1 570 kg	-	-	-	981 kg	-	-	-
Support Structure	4 320 kg	-	-	-	2 100 kg	-	-	-
Concentrator	739 kg	-	1 056 kg	-	3 010 kg	985 kg	385 kg	-
Foundation	1 092 kg	-	-	13 m ³	804 kg	-	-	10 m ³
Total Weight	7 721 kg	-	1 056 kg	13 m ³	6 895 kg	985 kg	385 kg	10 m ³
Specific Weight	73.5 kg/m ²	-	10 kg/m ²	124 l/m ²	46 kg/m ²	6.6 kg/m ²	2.6 kg/m ²	66.7 l/m ²

7 Realization of Constructive Improvements

As seen above, the performance of the large area heliostat could be greatly improved with some rather simple and inexpensive additions to the existing structure. This was done in a second step of this study. Considering the obtained results and suggestions of improvements, the stay pole idea was followed and elaborated.

7.1 Planning of the Construction

Fig. 7-1 gives an overview of the construction as it was planned and implemented.

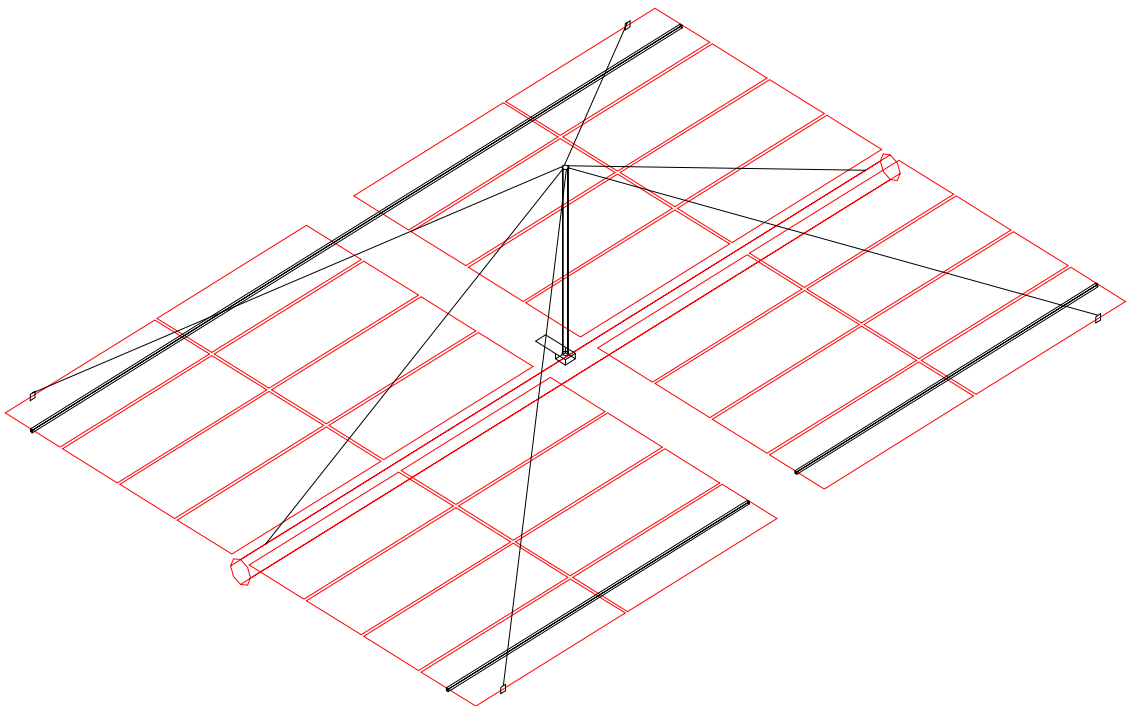


Fig. 7-1: Overview of the Stay Pole Construction

As known, the main deformations occur in the torque tube, therefore the tension should be mainly reduced by the two connections from the stay pole to the torque tube. Cables have only about half the Young's Modulus of solid steel /CASAR 1998/, that means they are twice as elastic and not advisable if stiffness is the main concern. Therefore, 16 mm solid steel bars were chosen.

The connections to the corners of the heliostat carry by far less weight and serve mainly to avoid the buckling of the stay pole and to reduce the wind effects, therefore 8 mm steel cables and 10 mm steel plates bolted to the corners were considered to be sufficient.

The stay pole itself consists of a 3 m long steel tube with a diameter of 90 mm and 5.5 mm walls. It was designed to surely bear the high pressure stresses without buckling.

The existing laser platform in the center of the torque tube was too weak to carry the high loads. It needed to be replaced by a new one which consists of a 600x200x20 mm steel plate with three

20 mm thick steel plates in double-T-arrangement as support (see Appendix). The long platform with 3 additional holes still allows the laser to be mounted, although slightly off center. The connecting parts like eyelet bolts, tension jacks, hooks, and rings were designed to bear the below mentioned forces in the tension units. The head part welded to the top of the pole was designed even stronger to surely avoid overstressing.

Square profiles were attached to the backside of the support structure in order to increase the stiffness by joining the previously separate facet rows. This avoids a tilting of the two heliostat branches in the mirror plane at low elevation angles and leads to a better distribution of the forces acting on single facets (wind, gravity, tension from the cables) to the whole structure.

The calculations of the forces in the tube, the bars and the cables were performed in R-Stab /R-STAB 1996/. With the above mentioned dimensions, the following results were obtained:

Table 7-1: Calculated Forces acting in the Staypole Construction

Force in cables	2 600 N
Force in bars	21 920 N
Force in pole	-25 000 N
Maximum displacement at 90° Elevation	4.1 mm

These values can be used to calculate the safety factors s of the parts that are subject to the highest stresses.

$$s_{cable} = \frac{F_{max}}{F_{cable}} = \frac{35900N}{2600N} = 13.8 \quad (7-1)$$

$$s_{bar} = \frac{F_{max}}{F_{bar}} = \frac{\sigma_{max} \cdot A}{F_{bar}} = \frac{300 \frac{N}{mm^2} \cdot (8mm)^2 \cdot \pi}{21920N} = 2.75 \quad (7-2)$$

$$s_{pole} = \frac{\sigma_{buckling}}{\sigma_{pole}} = \frac{\pi^2 \cdot E \cdot I_y}{l_k^2 \cdot F_{pole}} = \frac{\pi^2 \cdot 210000 \frac{N}{mm^2} \cdot 1308666mm^4}{(0.7 \cdot 3000mm)^2 \cdot 25000N} = 24.6 \quad (7-3)$$

The obtained safety factors are well above the usually used factors 1.2÷2.0 for tension loads and factors 5÷10 for buckling. This makes the structure safe even in case of manufacturing irregularities and for higher dynamic loads on windy days.

The parts needed to be manufactured are shown in detail in the Appendix. Except of the square profiles that were cut and drilled directly on the PSA, all the parts were ordered in a ship workshop in the port of Almería. The welding of the platform and the welding of head piece and footing to the tube was done in a workshop in Tabernas, a town close to the test site. The connection plates of the profiles and the bars were welded directly on the PSA.

Standard parts like cables, eyelet bolts, tension jacks, hooks, and rings were bought in a hardware shop. The needed parts, their amount and their cost can be seen in the written order below (see Table 7-2).

Table 7-2: Written Order for Construction Parts

descripción	cantidad	precio	importe
cancamo macho M20	2	400	800
cancamo macho M12	8	250	2 000
cable acero 8mm	34	150	5 100
tensor 5/8"	2	1 090	2 180
tensor 1/2"	4	576	2 304
sujeta-cable 5/16"	16	56	896
guardacabos 2"	8	52	416
tornillo M10x100	8	41	328
arandelas planas M10	16	1.5	24
tuerca hexagonal M12	16	5.4	86
tuerca hexagonal 5/8"	4	17	68
arandelas planas M12	32	2.5	80
tuerca hexagonal M16	4	11	44
tornillo M8x40	8	12	96
arandelas planas M8	8	0.9	7
cancamo hembra M16	4	325	1 300
grilletes 5/8"	4	555	2 220
brida d.210	1	}	
chapon de 600x400x20	1		
piezas de 100x100x20	4	}	32 500
piezas de 240x100x20	2		
pieza de 200x60.7x20	1	J	
chapas de 100x100x5 taladradas	4	}	
chapa 200x100x40	1	}	27 570
redondos d.16x6000 con roscas	2	J	
tubo std 3", 3 metros	1		9 780
total bruto			87 799
IVA			14 048
total factura			101 847

Due to the unique fabrication of the non-standard parts especially for the GM-100 prototype, the total costs of 101 847 Ptas (≈ 700 US\$) for the whole construction are by far higher than they would be in mass production. Nevertheless, even these costs could be compensated with the savings of a thinner torque tube (4 mm instead of 16 mm wall, see chapter 6.4.5) and the respective material savings of roughly 1 400 kg of steel.

7.2 Building of the Construction

The mounting of the construction was performed with the heliostat in face down position, this way the risk of damaging the facets was minimized and the work could be performed in lesser heights.

The platform, with the tube already connected by means of screws, was oriented perpendicular to the mirror plane and welded directly on the torque tube. The links at the outer ends of the torque tube consist of simple chain links that had been cut in two pieces and welded to the surface. The links in the corners of the heliostat were bolted to the square profiles of the facet support structure. The eight holes that needed to be drilled for that reason were the only alteration of the existing structure.

The square profiles were fixed with existing screws on the backside of the structure and connected in face down position, because in this position there is no tilting of the two branches away from each other.

With all these parts mounted, the cables and bars were connected and slightly tensioned in facedown position. In this position the deformations of the structure unstress the cables, hence it is ensured that they are always in tension when the heliostat is later turned to operating elevation and the tension in the cables and bars grows.

To prevent the new parts from corrosion, all parts except the stainless steel cables were degreased and painted twice. All the parts were painted white like the heliostat except the stay pole that was painted black. This should make the tube heat up and expand more and so compensate the unwanted lengthening of the bars and cables due to temperature rise when they are illuminated twice (direct sunlight and reflected sunlight).

Unfortunately, a bad weather period, several unforeseen problems in other projects of the PSA that needed to be solved, and the long absence of the responsible canting specialist due to illness made it impossible to comply with the tight schedule. At the end the heliostat could not be recanted.

The completely assembled stay pole construction is shown in Fig. 7-2.

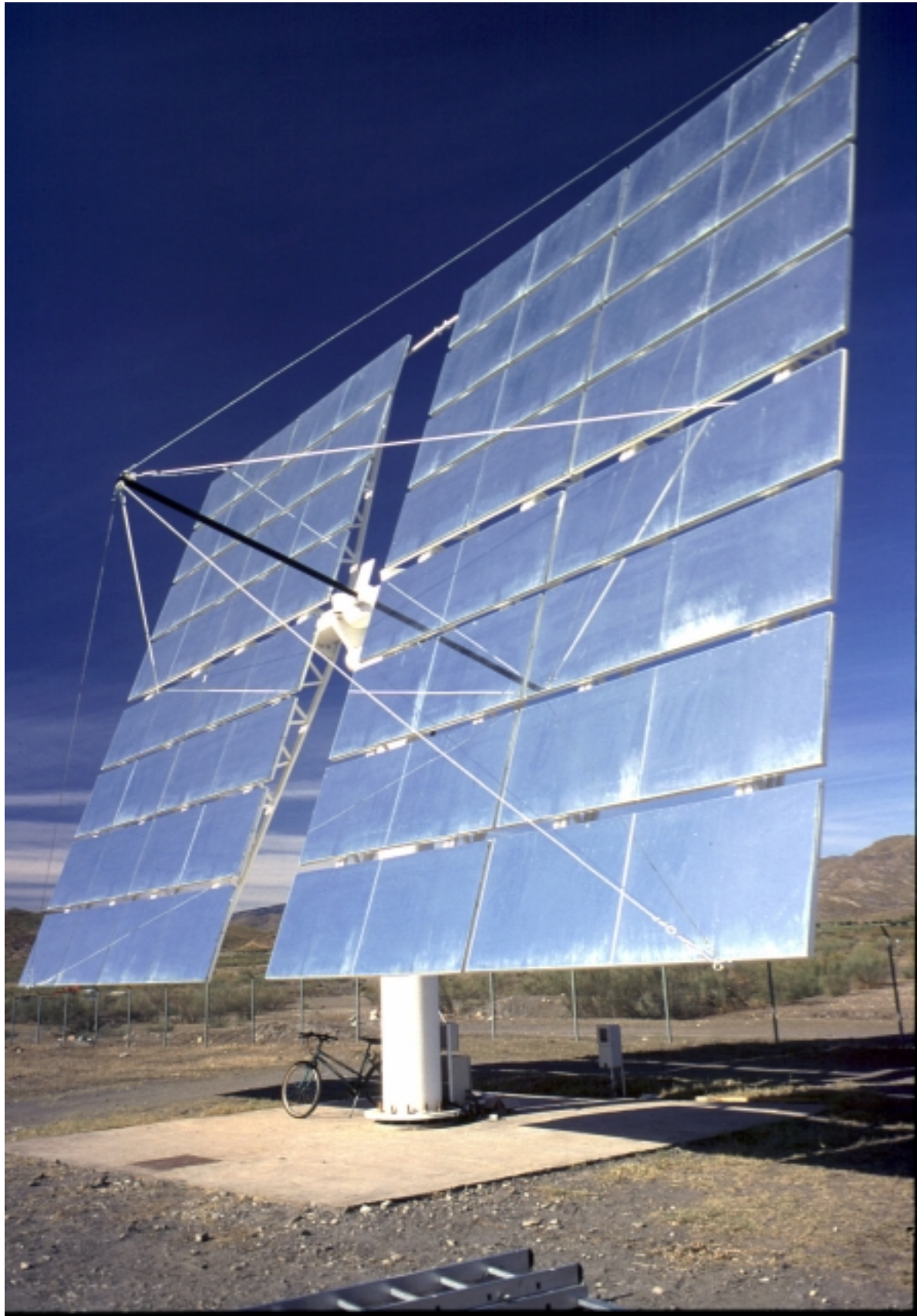


Fig. 7-2: The completely assembled Stay Pole Construction

7.3 The Testing of the Improved Construction

To judge the performance and improvement of the new construction, the same measurements as earlier are taken again. These are the Δz -deformations of the torque tube and the corners at the extreme heliostat positions face down/ face up, the temperature measurements and the daily focus development.

Table 7-3 shows the measured and calculated deformations of the original GM-100 as well as of the improved GM-100. The measurement points 1 to 4 are the same points like earlier (see Fig. 5-2). The originally calculated 9.7 mm deflection at the outer ends of the torque tube (points 1 and 2) was predicted to decrease by about 5.6 mm to 4.1 mm. The laser measurements of the original structure yielded 7 mm, almost 3 mm less than predicted, just like the measurements of the improved heliostat that yielded $1 \div 1.5$ mm, also about 3 mm less than predicted. This may be due to inaccuracies of the mathematical model or measurement inaccuracies or even hint at a measurement error, nevertheless, it validates the reduction of the deflection of $5.5 \div 6.0$ mm.

For the outer corners of the heliostat (points 3 and 4) there are no calculated values available, but the measurements show a great reduction of the heliostat deformations. The originally measured 9.5 mm were reduced by about 8.5 mm to only 1 mm.

This shows that the predicted improvement of the stiffness of the new heliostat not only became true, but is even more than expected.

Table 7-3: Measured and Calculated Deformations of Improved GM-100

	Original GM-100, April 21 st		Modified GM-100, December 9 th	
	measured	calculated	measured	calculated
Δz point 1	± 7 mm	± 9.7 mm	± 1 mm	± 4.1 mm
Δz point 2	± 7 mm	± 9.7 mm	± 1.5 mm	± 4.1 mm
Δz point 3	± 9.5 mm	± 11.4 mm	± 1 mm	-
Δz point 4	± 9.5 mm	± 11.4 mm	± 1 mm	-

The deformation improvements were calculated without any temperature influences. If the cables and bars that carry the tension load became very warm due to the double insolation (direct and reflected rays), they would lengthen and hence minimize the effect. Therefore, the bars were painted white and the stay pole was painted black in order to heat up more and so compensate for the bar lengthening. Table 7-4 shows the measured temperatures:

Table 7-4: Results of the Temperature Measurements on November, 26th, 1998

T_{ambient}	20°C
Insolation	870 W/m ²
$T_{\text{staypole (inner half)}}$	24°C
$T_{\text{staypole (outer half)}}$	26°C
T_{cable}	26.7°C
T_{bar}	22.5°C

November 26th was a completely sunny autumn day with an ambient temperature of 20°C and a direct insolation of 870 W/m² at the time of measurement. The heliostat was set in tracking mode the whole morning and at solar noon (13:00 h) the temperature measurements were taken. The black staypole, although almost parallel to the sunrays, had a mean temperature of 25°C, i.e. 5°C above ambient temperature. The cables heated up to 6.7 K above ambient temperature,

mainly because they are not painted white. The critical parts are the two steel bars that carry most of the load. Due to their white cover they had a temperature of 22.5°C, only 2.5 K above ambient temperature. This leads to differences in length of the bars and stay pole of only about 0.2 mm respectively and an almost exact compensation of the lengthening of the bars with the lengthening of the stay pole.

The measurements of the focus development during a whole day could not be taken because it was not possible to re-cant the heliostat in time. Therefore, only the calculations of the improved focus can be performed.

Fig. 7-3 shows the calculated focus development of the modified GM-100 on a typical winter day. It was supposed that the heliostat was recanted at a sun elevation angle of 30° (winter) and as input for the calculation, the calculated deformations of the improved heliostat with a maximum of 4.1 mm at its outer ends and the elevation and azimuth angles of the sun on December, 10th (Table 7-5) were taken. Temperature influences were not considered. A much better focus shape during the whole day can be observed. However, this is not only thanks to the improved construction, but also due to the reduced elevation and azimuth angles of the sun. This reduces the induced off-axis optical errors and the range of elevation angles of the GM-100.

A better comparison to the original focus development gives Fig. 7-4. Here, the same angles and temperature angles as earlier were used (June, 9th and July, 6th, see Fig. 6-2 and Fig. 6-8). It still shows some focus widening shortly after sunrise (9:18 h) and very close to sunset (19:44 h), but it is significantly reduced. Especially during the six hours around solar noon, the calculations show a very pleasing, circular focus spot.

Table 7-5: Sun Positions on December 10th 1998

Time	Elevation	Azimuth
9:10h	9.1°	52.3°
10:10h	17.9°	41.2°
11:10h	24.7°	28.3°
12:10h	29.0°	13.5°
13:10h	30.2°	-2.3°
14:10h	28.1°	-18.0°
15:10h	23.0°	-32.2°
16:10h	15.5°	-44.6°
17:10h	6.3°	-55.2°

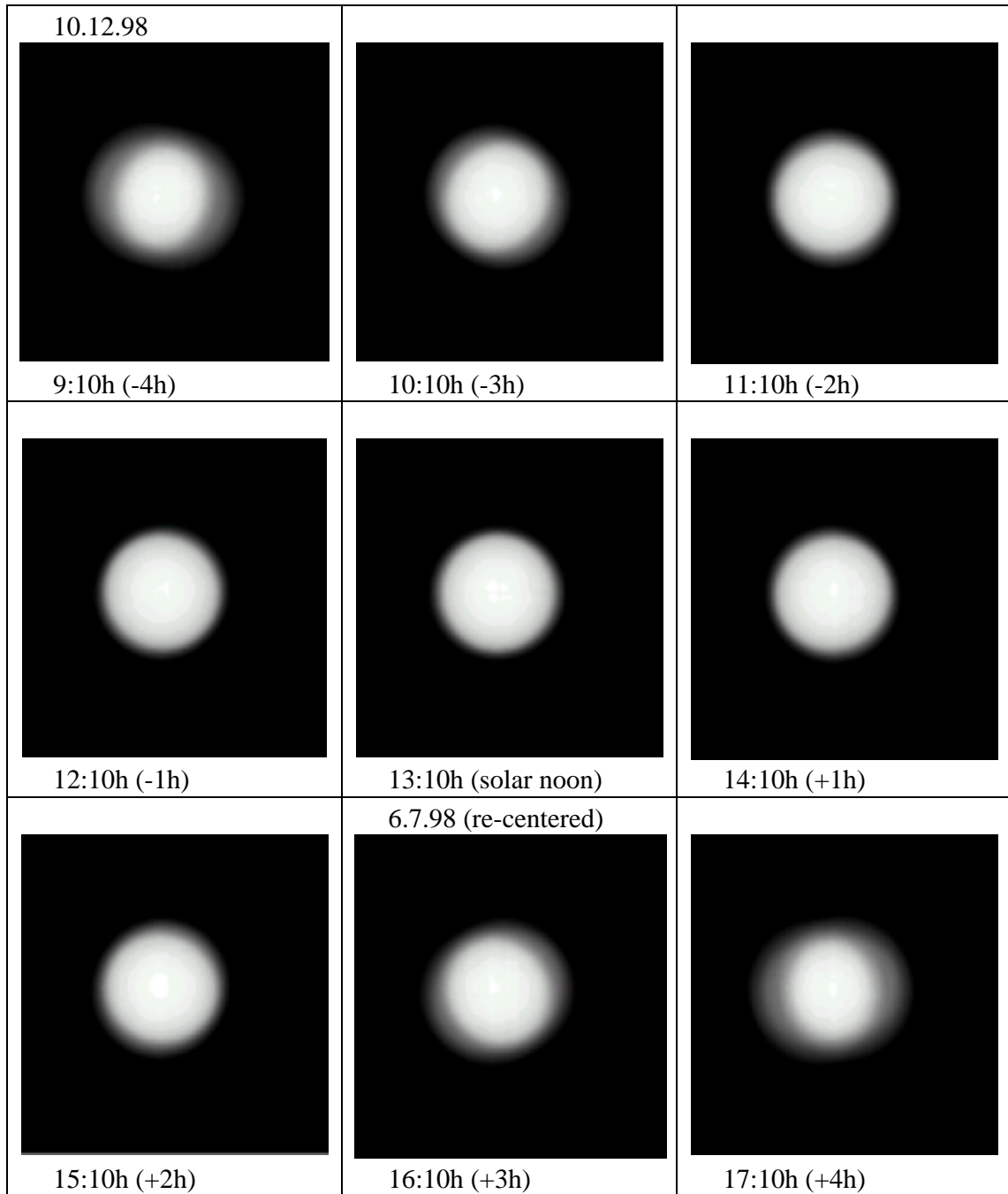


Fig. 7-3: Calculated Focus Development for modified GM-100 on December 10th 1998

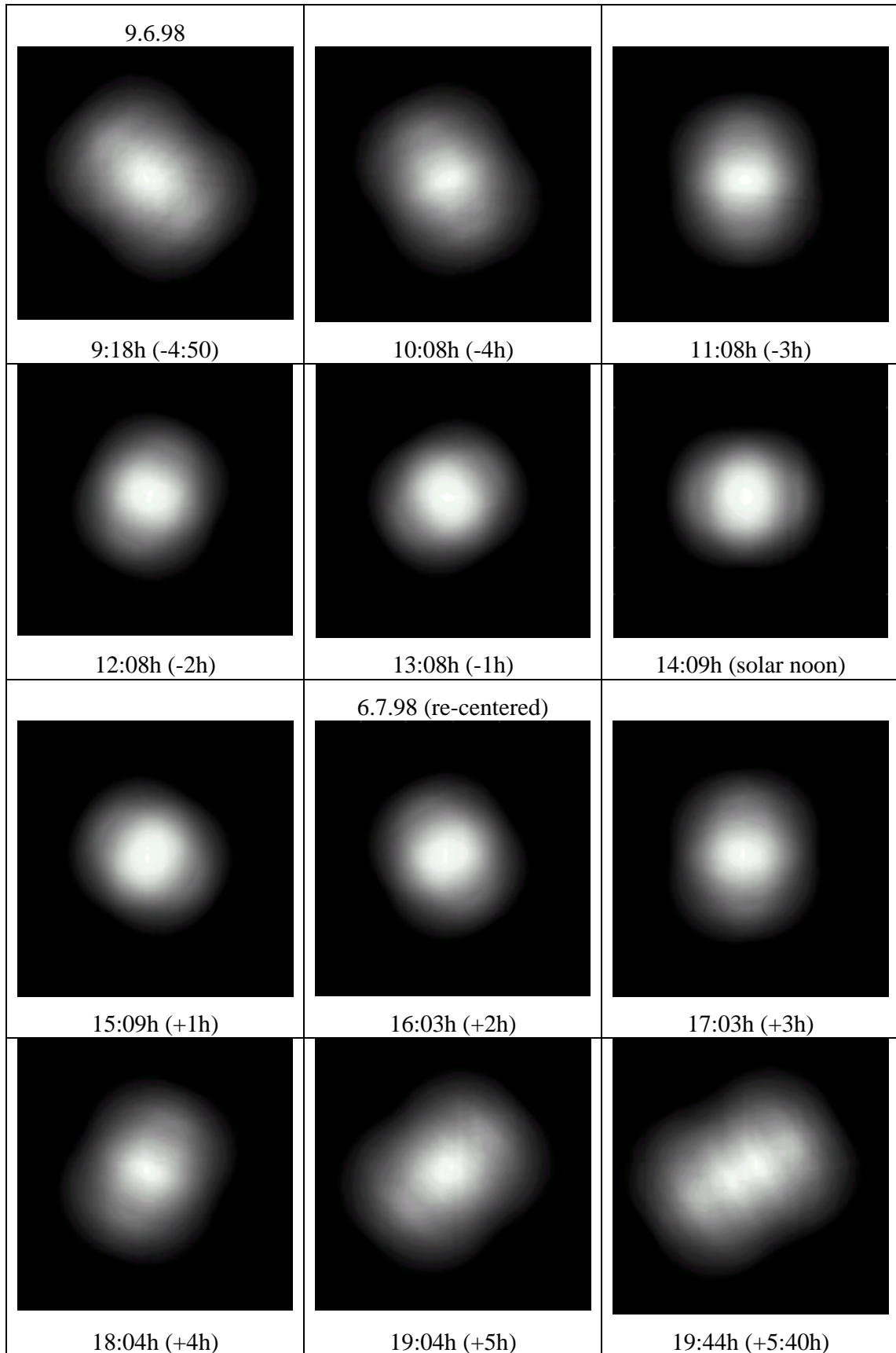


Fig. 7-4: Calculated Focus Development of the Modified GM-100 on June, 9th and July, 7th resp.

Due to off-axis optical errors, even an ideal concentrator cannot produce an ideal focus at off-noon hours. For this reason, Fig. 7-5 shows the GM-100 focus spot close to sunset compared to the theoretical ideal. The same input as earlier was used:

- heliostat canted at solar noon on July, 18th 1997 (elevation angle 38°)
- sun position for July, 6th 1998, 19:44 h (see Table 6-5)
- only deformations due to gravity considered

Fig. 7-5 a) shows the widely split up focus spot of the original GM-100. The focus improvement of the heliostat with the stay pole construction can be seen in Fig. 7-5 b). For this calculation, the theoretical deformations of the improved construction were used as data input (i.e. a maximum deformation of 4.1 mm at the outer end of the torque tube was supposed). Finally, Fig. 7-5 c) shows the image of an ideally shaped GM-100 heliostat. Here, the widening and tilting of the focus is only due to optical aberrations and off-axis astigmatism that become more apparent for large-area heliostats. In comparison, it can be clearly seen that the focus of the heliostat with stay pole construction is much closer to the theoretical optimum than the original one and therefore makes up a true improvement.

Faceted glass-metal heliostats are usually canted in an elevation angle close to solar noon at spring equinox in order to get an optimum performance of the heliostat seen over the whole year. The stay pole construction not only reduces the focus widening at higher elevation angles than the canting angle (summer months) and at lower elevation angles than the canting angle (winter months, off-noon hours), but also gives the possibility to alter the focal length in certain limits. By tensioning the cables and bars, the heliostat closes up (reduces its focal length) and can so compensate for the opening up at high elevation angles in the summer months. In winter the heliostat does not reach very high elevation angles, therefore it closes up and produces the known split up focus. This could be very easily compensated by relaxing the tension in the bars and cables (increasing the focal length) and so improve the heliostat performance.

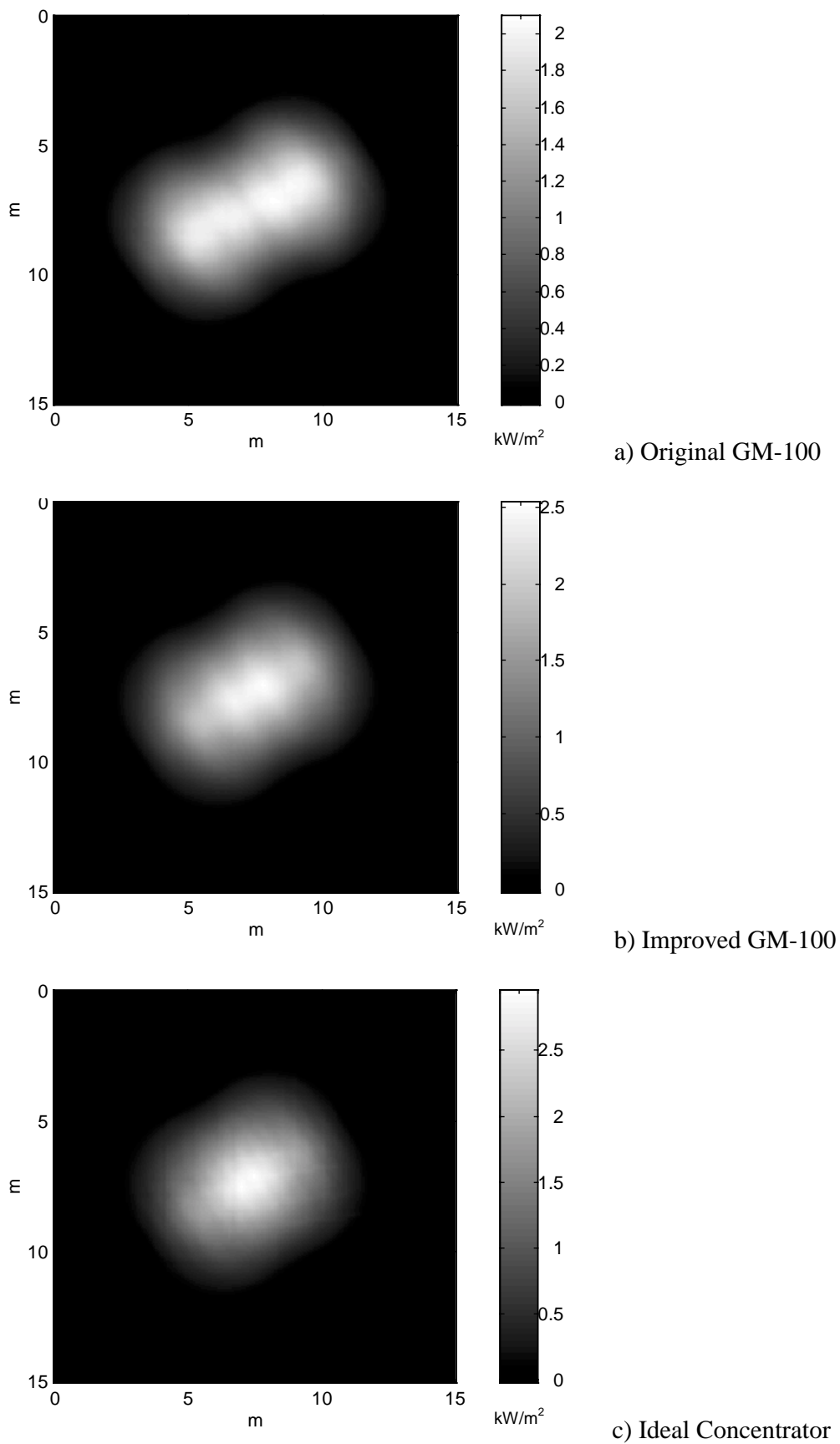


Fig. 7-5: Comparison of Calculated Focus Shapes close to Sunset (6.7.1998, 19:44h, DNI = 1.0 kW/m²)

8 Summary and Outlook

The largest single cost element of a solar power tower plant is with 30-50 % of the total investment cost the heliostat field. Therefore, significant effort has been devoted to lowering the specific costs of heliostats. As seen, this can be done most effectively by reducing their specific weight and so their direct material costs and by going to larger unit sizes and so reduce the number of needed drives, controls, foundations, etc. for a given plant size.

However, at the examined GM-100 and at other large-area heliostat prototypes in California this lead to unwanted reductions of the beam-quality. The GM-100 exhibits a notable focus widening especially in the off-noon hours early in the morning and at late afternoon. All possible reasons for this behavior were thoroughly considered and it was deduced that the main reasons are the deformations of the heliostat support structure under changing elevation angles due to gravitational loads and due to temperature gradients in the structural parts.

To analyze these deformations theoretically, the support structure was modeled in three separate parts: pedestal, torque tube and trusses. The applied loads vary depending on the elevation angle and the temperature gradients in the parts. Adding the deformations of the single parts up, a formula for the deflection of the reflective area depending on the elevation angle and the temperature gradients in the pedestal and the torque tube was obtained. This was used to determine the maximum deformations at specific points and as input for a program code to determine the theoretical daily focus development on the target.

In order to verify the calculated results, various measurement techniques were thought out and applied.

The laser set-up usually used for the canting procedure proved to be a very good tool to directly measure the deflection of the heliostat mirror surface. The theoretically predicted maximum deformation of the torque tube is with ± 9.7 mm in acceptable accordance with the measured ± 7 mm. The calculated additional deflection of the trusses of ± 2.6 mm is validated by the measurements of ± 2.5 mm.

The performed temperature measurements show that there may occur temperature differences of more than 5 K between the sunny sides and the back sides of the support structure tubes although they are painted white. The relation between temperature gradient and deformation (1 K temperature difference correspond to about 0.5 mm at the outer ends of the torque tube) was also validated.

With the help of the Prohermes flux measurement system it was possible to take pictures of the flux distribution on a target in given time intervals. They clearly show the splitting and tilting of the GM-100 focus during the day. By comparing them with the calculated daily focus development, a very good correspondence could be observed. This showed that in spite of its simplicity the mathematical model of the heliostat is a very good approximation of the actual deformations and it revealed that the main reason for the focus splitting is the excessive deflection of the torque tube.

Knowing this, several possibilities for the reduction of the torque tube deformations without adding more weight to the support structure were thought out. Their effects on the improvement of the beam-quality were estimated and compared. The most promising idea that could be still added to the existing prototype was chosen, planned and realized. A construction with a stay pole and tensioned steel bars and cables to reduce the stresses in the torque tube was erected. This was estimated to reduce the deformations of the torque tube by more than 50 % to a maximum of

4.1 mm. The deformation measurements taken with the laser set-up not only validated the predicted improvements but lead to even lower values (± 1.5 mm). This is not completely consistent with the estimated values, nevertheless it can be said that with the tested stay pole construction it is possible to reduce the deflections of the heliostat greatly and so improve its beam-quality significantly. Unfortunately, the pictures on the target of the improved focus development during a whole day could not be taken because it was not possible to re-cant the heliostat in time.

Additionally, the construction permits a reduction of the wall thickness of the torque tube from 16 mm to 4 mm with an equally good beam-quality which corresponds to a weight reduction of about 1400 kg of steel. Furthermore, the altering of the cable tension allows the quick optimization of the heliostat performance for changing sun elevations in different seasons.

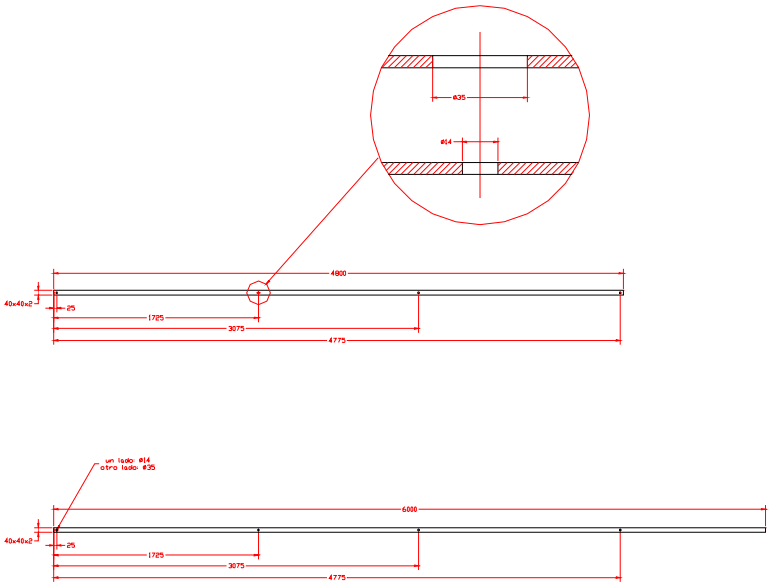
With all these advantages, low-cost large-area heliostats with stay pole construction can contribute to the cost reduction of future solar power tower plants and hence help them on their way to enter the world-wide energy market.

9 References

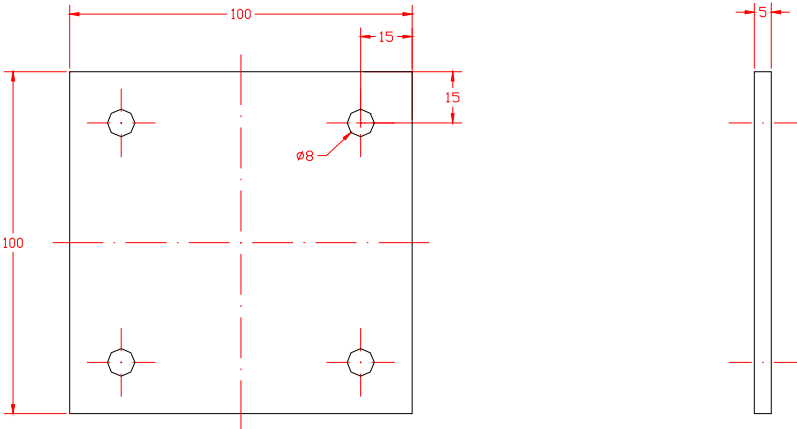
- /ANSYS 1997/ “Multiphysics Capabilities of ANSYS”, Ansys Inc., Canonsburg, PA, USA, 1997
- /BAEHR 1996/ Baehr: “Thermodynamik”, 9. Auflage, Springer Verlag, Berlin, 1996
- /BECKER 1993/ Becker, M., Klimas, P.: “Second Generation Central Receiver Technologies - A Status Report”, Verlag C.F. Müller, Karlsruhe, 1993
- /BROWN 1991/ Brown, D., Konnerth, A., Schertz, P., White, D.: “Design and Cost of the First Commercial Stretched-Membrane Heliostat”, Sandia Report SAND90-7038 UC-235, Sandia National Laboratories, Albuquerque, New Mexico, July 1991
- /BURCH 1998/ Burch, G. D., Rueckert, T. L.: “Concentrating Solar Power, Five Year Program Plan 1998-2003”, U.S. Department of Energy, 1000 Independence Avenue, SW, Washington DC, April 1998
- /CASAR 1998/ Produktinformations-CD, CASAR Drahtseilwerk Saar GmbH, Casarstr. 1, 66459 Kirkel-Limbach, 1998
- /CIEMAT 1994/ Moreno, G. B.: “Helióstatos de 100m² Diseño Faceta”, Centro de Investigaciones Energéticas, Medioambientales y Tecnológicas (CIEMAT), Madrid, 1994
- /CIEMAT 1996/ Solar PACES Report III-5/95, “Solar Thermal Test Facilities”, Centro de Investigaciones Energéticas, Medioambientales y Tecnológicas (CIEMAT), Madrid, March 1996
- /DUBBEL 1986/ Beitz, W., Küttner, K.-H.: “Dubbel - Taschenbuch für den Maschinenbau”, 15. Auflage, Springer Verlag, Berlin, Heidelberg, 1986
- /ERBE 1997/ Erbe, C.: “Bilanzierung der Stoff- und Energieströme von Heliostaten”, Studienarbeit, Universität Stuttgart, IER Band 272, Juni '97
- /FALCONE 1986/ Falcone, P. K.: “A Handbook for Solar Central Receiver Design”, Sandia Report SAND86-8009 UC-62a, Sandia National Laboratories, Albuquerque, New Mexico, December 1986
- /FINKENWIRTH 1997/ Finkenwirth, O.: “Realization and Evaluation of Flux Density Measurements”, Studienarbeit, Plataforma Solar de Almería, Apartado 22, E-04200 Tabernas (Almería), Spain
- /GLAHN 1998/ Glahn, W.: “Steuerung und Charakterisierung eines Stretched Membrane Heliostatspiegels ASM 150”, Diplomarbeit, Plataforma Solar de Almería, Apartado 22, E-04200 Tabernas (Almería), Spain, 1998
- /GOLDBERG 1991/ Goldberg, V. R., Ford, J. L., Anderson, A. E.: “Design of the Support Structure, Drive Pedestal, and Controls for a Solar Concentrator”, Sandia Report SAND91-7007 UC-237, Sandia National Laboratories, Albuquerque, New Mexico, August 1991
- /HELIOS 1979/ Biggs, F., Vittitoe, C. N.: “The HELIOS Model for the Optical Behavior of Reflecting Solar Concentrators”, SAND76-0347, Sandia National Laboratories, Albuquerque, New Mexico, 1979
- /HOLLÄNDER 1998/ Holländer, A., Kröger-Vodde, A.: “CCD Flux Measurement System PROHERMES”, 9th International Symposium on Solar Thermal Concentrating Technologies, Odeillo, France, 1998
- /JOHANSSON 1993/ Johansson, T. B., Kelly, H., Reddy, A. K. N., Williams, R.: “Renewable Energy - Sources for Fuels and Electricity”, Island Press, 1993
- /KUSSMAUL 1994/ Kussmaul, K.: “Festigkeitslehre I”, Vorlesungsmanuskript, Staatliche Materialprüfungsanstalt, Universität Stuttgart, 1994
- /MAGNUS MÜLLER 1990/ Magnus, K., Müller, H. H.: “Grundlagen der Technischen Mechanik”, Teubner Studienbücher Mechanik, 6. Auflage, B. G. Teubner Stuttgart 1990
- /MARTIN MARIETTA 1982/ Martin Marietta Corporation, Contractor Report: “Second Generation Heliostat Optimization Studies”, Sandia Report SAND82-8175 UC-62d, Sandia National Laboratories, Albuquerque, New Mexico, May 1982

- /MAVIS 1989/ Mavis, C. L.: "A Description and Assessment of Heliostat Technology", Sandia Report SAND87-8025 UC-235, Sandia National Laboratories, Albuquerque, New Mexico, January 1989
- /MONTERREAL 1996/ Monterreal, R.: "A new On-axis Canting Method for Faceted Heliostat", Solar Thermal Concentrating Technologies, Volume 2, Proceedings of the 8th International Symposium, October, 6-11 1996, Köln, Germany
- /MONTERREAL 1997/ Monterreal, R., Heller, P.: "Large Area Heliostat Comparison at PSA", Plataforma Solar de Almería, Apartado 22, E-04200 Tabernas (Almería), Spain, November 1997
- /MONTERREAL 1997/ Monterreal, R., Romero, M.: "Development and Testing of a 100m² Glass-Metal Heliostat with a new Local Control System", Solar Engineering ASME 1997
- /MONTERREAL 1998/ Monterreal, R., private communication, 1998
- /OPTIMAS 1996/ OPTIMAS Users Guide and Technical Reference Vol. I+II, 8th Edition, Optimas Corporation, Bothell, USA, 1996
- /ORIGIN 1997/ Microcal Origin Version 5.0, Microcal Software Inc., Northhampton, MA, USA, 1997
- /PITZ-PAAL 1997/ Pitz-Paal, R., Buck, R., Schmitz-Goeb, M., Weinrebe G.: Solarturmkraftwerke, Forschungsverbund Sonnenenergie "Themen 1996/97"
- /PSA 1996/ "Plataforma Solar de Almería: Annual Technical Report 1996", CIEMAT, DLR, Plataforma Solar de Almería, Apartado 22, E-04200 Tabernas (Almería), Spain, 1996
- /PSA 1997/ "Plataforma Solar de Almería: Annual Technical Report 1997", CIEMAT, DLR, Plataforma Solar de Almería, Apartado 22, E-04200 Tabernas (Almería), Spain, 1997
- /REFOS 1998/ Project Description REFOS, DLR-Solarthermie-Internet-Homepage <http://www.st.dlr.de/en/tt/solartherm/refos/refos.html>
- /R-STAB 1996/ R-Stab Version 3.67 Student, Ingenieur-Software Dlubal GmbH, Tiefenbach, Deutschland, 1996
- /SÁNCHEZ 1996/ Sánchez, M., Romero, M., Ajona, J.: "Sensitivity Analysis of a Hybrid Solar Tower Plant for Southern Spain", Proceedings of the 8th International Symposium, October, 6-11, 1996, Köln, Germany
- /SCHMITZ-GOEB 1996/ Schmitz-Goeb, M., Finker, A.: "The PHOEBUS Solar Power Tower", Solar Thermal Concentrating Technologies 1996
- /STEINMÜLLER 1995/ L.&C. Steinmüller GmbH: "PHOEBUS Solar Power Tower", Gummersbach. Germany, 1995
- /STRACHAN 1993/ Strachan, W., Houser, R. M.: "Testing and Evaluation of Large-Area Heliostats for Solar Thermal Applications", SAND92-1381 UC-235, Sandia National Laboratories, Albuquerque, New Mexico, 1993
- /STRACHAN 1994/ Strachan, J. W., Van Der Geest, J.: "Operational Experience and Evaluation of a Dual-Element Stretched-Membrane Heliostat", Sandia Report SAND93-2453 UC-235, Sandia National Laboratories, Albuquerque, New Mexico, January 1994
- /WEINREBE 1998/ Weinrebe, G., Böhnke, M., Trieb, F.: "Life Cycle Assessment of an 80 MW SEGS Plant and a 30 MW PHOEBUS Power Tower", Proceedings of the ASME 1998 Conference on Solar Energy, Albuquerque, NM, June 13-17, 1998
- /WILLIAMS 1987/ Williams, T. A. u.a.: Characterization of Solar Thermal Concepts for Electricity Generation, Pacific Northwest Laboratory / Batelle Memorial Institute, PNL-6128 Vol. 1, Richland, Washington, 1987
- /WINTER 1991/ Winter, C.-J., Sizmann, R. L., Vant-Hull, L. L.: "Solar Power Plants: Fundamentals – Technology – Systems - Economics", Springer-Verlag Berlin, Heidelberg 1991

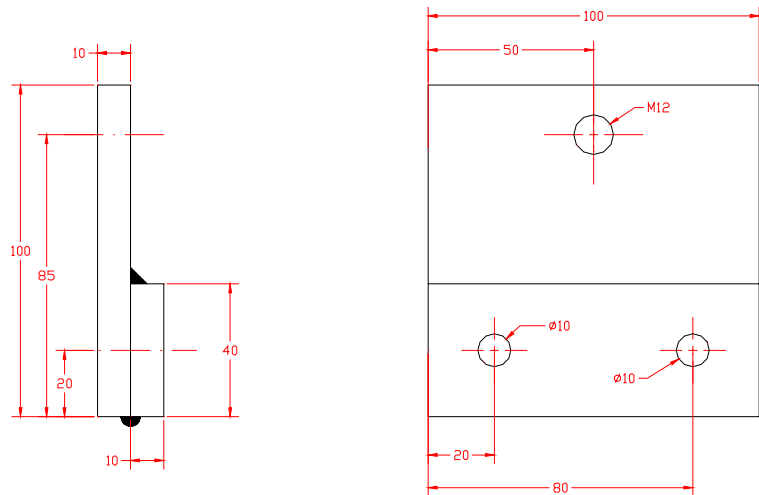
Appendix



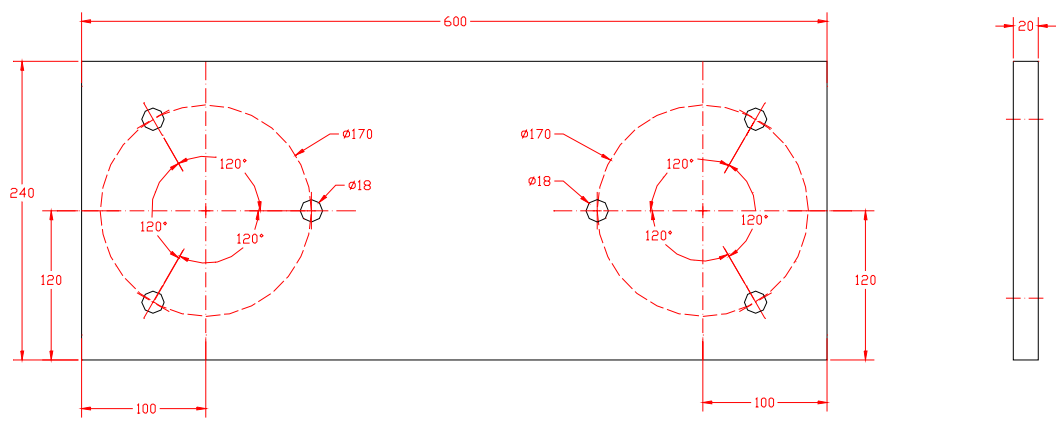
Square Profiles for Backside Reinforcement (2x each)



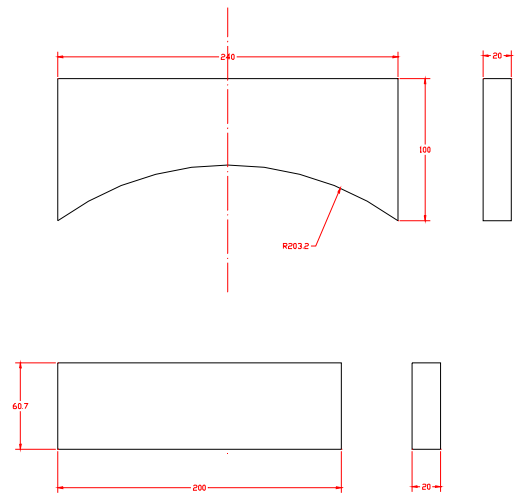
Linking Plates of Square Profiles (4x)



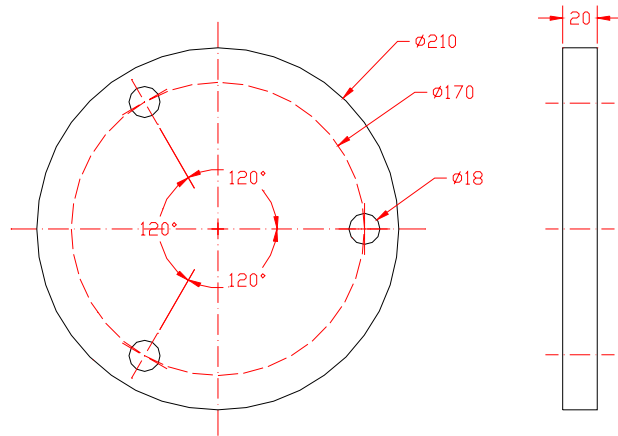
Plates for Diagonal Wiring



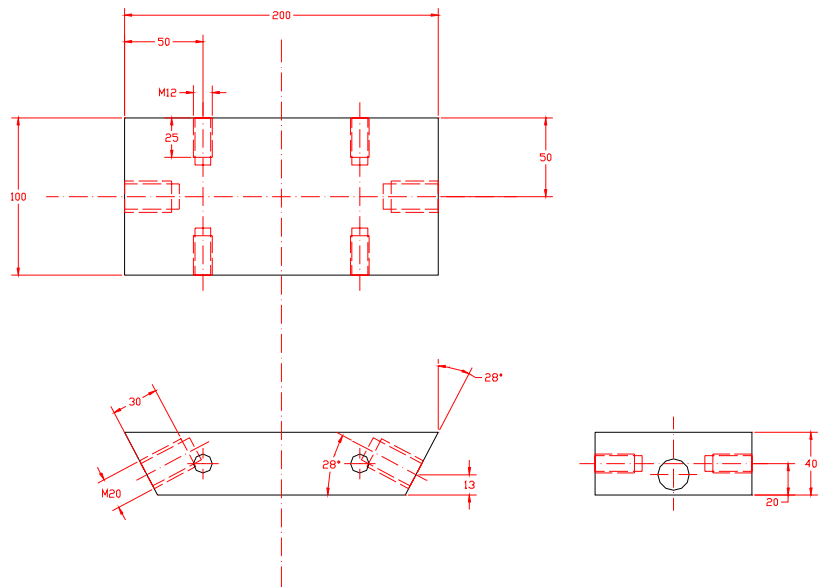
Platform Steel Plate with Seats for Stay Pole and Laser



Platform Support



Tube Footing



Tube Head Piece